PHYSICAL REVIEW B VOLUME 47, NUMBER 22 1 JUNE 1993-II

Collective motion of quantized vortex lines in rotating superfluid ^{3}He-*B*

M. Krusius, J. S. Korhonen, Y. Kondo,* and E. B. Sonin†
Low Temperature Laboratory, Helsinki University of Technology, 02150 Espoo, Finland

(Received 22 October 1992)

Insight in the dynamics of quantized vortex lines has been obtained by performing NMR measurements in uniformly rotating superfluid ^{3}He-*B*. Compared to superfluid ^{4}He, in ^{3}He-*B* the viscosity of the normal component is three orders of magnitude larger and the pinning of vortices is weaker. The collective modes governing the hydrodynamic response of an array of vortex lines are highly overdamped. Two distinct modes are identified: (1) a relatively fast mutual-friction-resisted mode, which controls the redistribution of the vortex density on a time scale of a few seconds, and (2) an exponentially relaxing slow mode with a time constant of a few minutes, which governs asymptotically the approach to equilibrium at nearly constant vortex density. Measurement of the fast motion allows us to extract the dissipative mutual friction. The slow mode is dominated by the elastic tension along the vortex line and by weak pinning at the top and bottom surfaces of the rotating container. With increasing vortex density the surface pinning becomes a collective process, in which coherently moving groups of vortices are pinned in unison. Collective pinning is a result of the shear elasticity related to the crystalline order of the vortex lattice. Our measurements on the slow mode indicate that the crystalline correlation extends over many lattice spacings.

I. INTRODUCTION

A. Vortex motion in rotating ^{3}He and ^{4}He superfluids

The simplest case, where quantized vortex lines are abundantly formed and can be studied, is uniform rotation of the superfluid at constant rotation velocity: Here vortices exist as a response to rotation, allowing the irrotational or curl-free superflow to accommodate to solid body rotation on an average scale.[1,2] Quantized vortices have been studied for four decades in superfluid ^{4}He, where their structure is simple and their properties in the equilibrium state are well established. In superfluid ^{3}He they have been investigated for the past ten years; here their structures are varied and complicated, but many of their equilibrium characteristics are now understood.[3–5] Quantized vortex lines have also been invoked as an explanation of the rotation characteristics of pulsars, i.e., rapidly rotating gravitationally collapsed stars where matter is compressed to a neutron superfluid.[6–8] In most experiments a large number of vortices has been studied, but quantization of circulation has been unambiguously proven in experiments with a single vortex trapped on a vibrating wire both in ^{4}He (Ref. 9) and in ^{3}He.[10]

In the uniformly rotating superfluid at constant rotation velocity Ω vortices form an array of rectilinear lines with homogeneous density. Our central theme here is the following question: What is the dynamic response of the array to an externally applied disturbance, such as a step change in Ω? A generally accepted consensus on the dynamic response of a vortex array and the nature of its collective modes is difficult to find in the existing literature on the hydrodynamics of quantized vortex lines in superfluid ^{4}He.[11–13] Superfluid ^{3}He is generally regarded as more complicated and diverse in its structure and properties than ^{4}He-II but there are several aspects which promise that studies on vortex dynamics in the ^{3}He superfluids may provide new understanding.[14]

(1) Measuring techniques. With ^{3}He powerful measuring techniques have become available for the investigation of the superfluid state, foremost NMR and zero sound transmission. NMR is generally regarded as a method for structural studies, but here we shall make use of an NMR measuring technique,[15] applicable in the *B* phase, which has proven most efficient for analyzing the dynamic properties of a vortex array.[16] In contrast, in superfluid ^{4}He the most successful dynamic measuring techniques have been based on ion methods.[17] The ions trapped to vortex cores can be driven and monitored[18,19] and even imaged.[20] Due to the large vortex core size in ^{3}He, the ionic trapping potential is much lower and it has not yet been possible to reach a satisfactory sensitivity.

(2) High nucleation threshold. In superfluid ^{3}He the critical flow velocity for the nucleation of singular vortex cores turns out to be relatively high.[21] In these circumstances uncontrolled nucleation and annihilation of vortices can be totally eliminated in the measurements, i.e., experiments can be carried out with a strictly constant number of vortices even if Ω is varied within wide margins.

(3) Regime of superfluid hydrodynamics. Compared to ^{4}He, in ^{3}He the viscosity of the normal component is more than 3 orders of magnitude larger: the kinematic viscosity ν of ^{4}He is roughly 10^{-4} cm^2/s ($T \approx 1$ K) while that of ^{3}He is 1 cm^2/s ($T \approx 1$ mK). As a result different types of slow vortex motion, i.e., motion with frequencies $\omega \ll \Omega$, are available for experimental observation in ^{3}He than in ^{4}He. In ^{4}He the normal and superfluid components and the vortices move together during the slow motion, i.e., all three are glued to each other by mutual friction.[22–24] In contrast, in ^{3}He the normal component can be considered to be clamped to corotation with the

container.[13]

(4) Weak surface pinning. In ^{3}He pinning is expected to be weaker than in ^{4}He due to the much larger core size. The radius r_c of the singular core is well above 10 nm, unlike in ^{4}He where the core radius is of atomic size (a few Å).

B. Central conclusions and outline of contents

The central result of this report is to conclude that the response of a vortex array to a perturbation can be described by two modes: a fast and a slow response, which are well separated in time. The existence and characteristics of these modes in superfluid ^{3}He-B we derive independently from the measured response and from the theoretical argumentation. These two modes are (1) a relatively *fast* mutual-friction-resisted mode, which governs the motion over large displacements with a time scale τ_F of order the rotation period, and (2) an exponentially damped slow mode with a relaxation time τ_s, which is responsible for small adjustments during the asymptotic approach towards new equilibrium sites. These two modes of vortex motion are present in the response of a vortex array to any disturbance, such as a step change in the rotation velocity Ω, as shown schematically in Fig. 1.

The fast and slow modes are fundamentally different. In the fast mode of importance is the radial motion which is responsible for equilibrating the vortex density. The slow motion is predominantly azimuthal in character and corresponds to the final relaxation of the deformed vortex pattern at equilibrium vortex density. Both motions are damped by mutual friction: The fast mode is dominated by mutual friction alone while the slow mode is additionally controlled by the elastic tension of the vortex lines and by surface pinning.

A long-standing problem is to what extent one should treat the array as an ordered vortex lattice.[25] The pinning parameter derived from the measured exponential relaxation time of the slow mode displays a dependence on the density of vortices. We interpret it using the concept of collective pinning, developed for bulk pinning in type-II superconductors.[26] Collective pinning is possible only if crystalline order exists in the vortex lattice; our observations are thus evidence for crystalline order which extends over many lattice spacings.

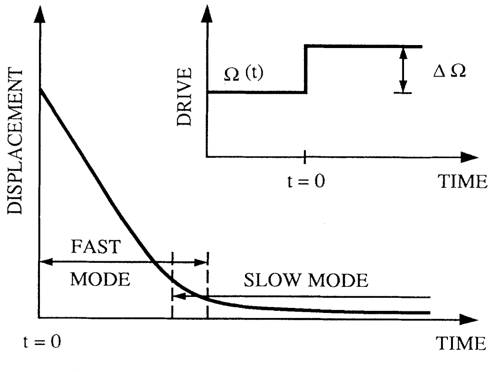

FIG. 1. The response of a vortex array to a rotation drive, which varies with time, is an overdamped relaxation in ^{3}He. Here the rotation velocity Ω is rapidly increased by an increment $\Delta\Omega$ (inset). Two different well-separable modes can be distinguished in the response: (1) The fast mutual-friction-resisted mode first approximately corrects the vortex density with a characteristic decay time $\tau_F \sim 1$ s. (2) Next the slow vortex mode with exponential relaxation and a time constant $\tau_s \sim 100$ s governs the approach to the new equilibrium state. The average displacement of the vortices from their final sites is here schematically illustrated as a function of time during the relaxation.

Our identification of the two modes is derived from the time dependences of the observed NMR signals. The existence of these modes with the time dependences and the time scales, which agree with the NMR results, unambiguously follows from existing hydrodynamic theory without any new assumptions, as we show in the present work. However, it is much less evident why the NMR signal is influenced by hydrodynamic motion during the exponential relaxation of the slow mode when the number of vortices is kept constant. We describe some features of this phenomenon,[16] but we are not yet prepared to present a complete analysis of the connection between the slow mode and the amplitude of the measured resonance signal. The experimental identification of the slow vortex mode is dictated by the time dependence of the NMR signal: we know of no process except for the hydrodynamic slow vortex mode that has a characteristic time relevant to the observed time scale.

The plan of the paper is the following. We start with a short description of the experimental setup in Sec. II and an account on vortex nucleation in Sec. III. An important precondition for measurements with a rotation drive varying in time is that the number of vortices can be kept constant. This is the case here, since nucleation is inhibited in the range of rotation velocities, where the slow mode is studied. Our NMR method is described in Sec. IV, where we characterize the resonance signals, which are measured as a response to fast and slow vortex motion.

The rest of the paper is devoted to the hydrodynamic theory and its comparison with the experiment. We start from a general introduction to vortex dynamics (Sec. V), then derive the fast (Sec. VI) and slow (Sec. VII) modes, which allows us to identify the experimental modes by comparing the results of the theory with measurements. Section VII is central for our present work. Here, on the basis of well known and widely used ideas of the elastic forces acting on a vortex (the line-tension force[27] and the force from shear deformation of the ordered vortex array[28,1,12,13]), we discuss the concept of and the experimental evidence for the collective surface pinning, which is related to the shear rigidity of the vortex array in the boundary layers near the top and the bottom of the rotating container.

A number of appendices are included in the report. They are devoted to those experimental results which need better quantitative theoretical interpretation or to the discussion of other questions which are not vital to the chain of arguments leading to the main conclusions of the present work. In Appendix A we discuss the coupling between the NMR signal and the slow vortex mode; it is based on the broken cylindrical symmetry of the vortex core. The interaction of the peripheral vortices of the equilibrium vortex cluster with the cylindrical container wall leads to peculiar NMR absorption behavior, which is described in Appendix B. New phenomena will become observable when vortices interacting at superfluid interfaces are studied: ^{3}He-B above a mixture of superfluid ^{4}He with 6.4% of normal ^{3}He will be briefly discussed in Appendix C. Next in Appendix D we discuss the bulk liquid contribution to the slow mode from the shear rigidity of the vortex lattice. In ^{4}He this contribution is responsible for the Tkachenko wave.[28] In ^{3}He the Tkachenko wave would transform into an overdamped mode. In the present experiment it was not observed; a positive identification of its existence would require a different experimental geometry.

Finally it should be pointed out that our general hydrodynamic considerations apply to both the A and B phases of superfluid ^{3}He. It is simply our experimental technique which has made these hydrodynamic features in the B phase more amenable to measurement: The particular NMR mode, which we use, couples with the slow vortex motion (see Sec. IV). Consequently, while our measurements and considerations are explicitly for ^{3}He-B in this work, no differences of fundamental nature separate the hydrodynamics of ^{3}He-B and other ^{3}He superfluids. In fact, our results pertain to any rotating superfluid with a large normal viscosity.

II. EXPERIMENTAL SETUP

The measurements are performed in a rotating cryostat which consists of a ^{3}He-^{4}He dilution refrigerator for precooling and a copper nuclear demagnetization stage for cooling the liquid-^{3}He chamber. The upper section of the ^{3}He chamber is shown schematically in Fig. 2. It is a cylindrical epoxy tower with its axis aligned along the vertically oriented rotation axis of the cryostat. The tower is constructed on a copper lid which is, in turn secured with an indium O ring on a silver chamber. This chamber houses the sintered silver heat exchanger for thermal contact to the nuclear stage. The tower is divided in two sections with an epoxy wall, which incorporates an orifice (diameter $=1$ mm, length $=0.5$ mm) and a tubular channel (diameter $=1.5$ mm, length $=$ 5.5 mm). This division isolates the NMR sample cell (diameter $2R=$length $L=7$ mm) from the lower parts of the ^{3}He volume, but provides a still acceptable thermal connection.

The transversely oriented rf coil around the NMR cell consists of two square sections, which are thermally anchored to the mixing chamber. The two sections of the coil each have 40 turns of copper wire giving the coil an inductance of 60 μH. One end of the coil is grounded inside the cryostat while the other end is fed via a coaxial cable to a room-temperature tuning capacitance. This assembly provides a Q value of 100 at 1 MHz. The rf excitation is fed directly in the ^{3}He-NMR coil from a constant current source. For compensating the large voltage induced by the excitation current, a second similar tank circuit is placed inside the cryostat. Each of the two tank circuits is connected to one input of a differential preamplifier. The preamplifier is followed by a lock-in amplifier, which is used as the readout instrument. With careful frequency tuning of the two tank circuits and adjustment of the relative phase and amplitude of their excitation currents, a compensation of up to a factor of 100 is achieved.

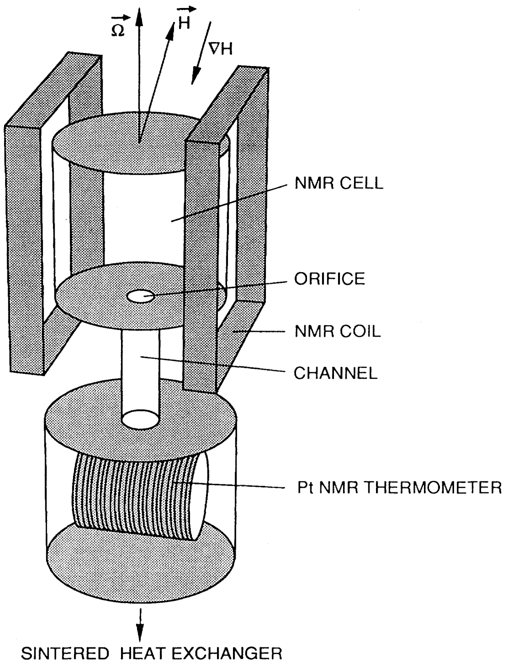

FIG. 2. Upper section of the ^{3}He sample chamber. The NMR cell on the top of the tower is isolated with an orifice and a tubular section from the main ^{3}He volume. The bottom surface of the main ^{3}He volume is the sintered heat exchanger (not shown), which provides thermal contact between the liquid-^{3}He sample and the copper nuclear refrigeration stage.

The rf coil for pulsed platinum NMR thermometry is immersed in the liquid below the division between the NMR cell and the rest of the ^{3}He volume. The steady NMR field, which is common for both the ^{3}He and ^{195}Pt NMR, and a linear field gradient are produced with large-size superconducting solenoidal coils, located in the liquid-He bath outside the vacuum jacket. The temperature is determined from the integrated intensity of the ^{195}Pt free-precession signal, which is calibrated at T_c. A second convenient calibration temperature is T_v, the temperature of the second-order phase transition in the vortex-core structure (see Sec. IV B). Most of the present measurements have been performed with the liquid pressure at $p=29.3$ bars, where $T_v=0.60T_c$.

The dividing plug in the ^{3}He tower with its narrow orifice prevents the leakage of vortices from the lower volume into the NMR cell. The NMR cell has relatively smooth epoxy walls and a smaller diameter, while the lower part has a rough heat exchange sinter as the bottom surface and a maximum diameter of 28 mm. The silver powder in the sinter has a nominal grain size of 70 nm, which roughly matches with the core size of singular vortices. The critical rotation velocity for vortex nucleation is thus reduced to ≤ 0.1 rad/s in the lower part of the cell. In contrast, in the NMR cell the critical rotation velocity $\Omega_c(T,p)$ for the nucleation of singular vortices in the B phase is $1-3$ rad/s, depending on pressure p and temperature T.[21] This provides a possibility to perform measurements on the dynamics of the vortex array in the presence of time varying rotation drives without complications from nucleation or annihilation of vortices.

III. VORTEX NUCLEATION AND A METASTABLE VORTEX CLUSTER

The critical rotation velocity $\Omega_c(T)$ for the nucleation of vortices in the B phase is shown in Fig. 3 at 21.0 and 5.0 bars. Ω_c translates to a critical flow velocity $v_{sc}=\Omega_c R$ of up to 1 cm/s at the cylindrical cell wall, where the nucleation takes place. This is approximately one-tenth of the bulk liquid pair-breaking velocity. Below the critical line $\Omega_c(T)$ vortex-free counterflow prevails and no vortices are nucleated. Above the critical line vortices are nucleated such that the counterflow velocity at the cylindrical cell wall $\leq v_{sc}$. $\Omega_c(T)$ can be identified from NMR measurements by scanning the Ω vs T plane by either increasing Ω isothermally or by sweeping T at constant Ω. During such a sweep a traversal of the critical line is indicated by an abrupt change in one of the several possible features in the NMR spectrum, which depend on the relative magnitude of counterflow compared to the total number of vortices.[21] Close to T_c on exceeding the critical rotation velocity Ω_c vortices are created essentially one by one. Towards lower temperatures the nucleation process transforms to a burstlike phenomenon, in which a large number of vortices are formed simultaneously. At the lowest temperatures $T<0.4T_c$ it appears that almost the entire NMR cell is filled at the nucleation threshold.

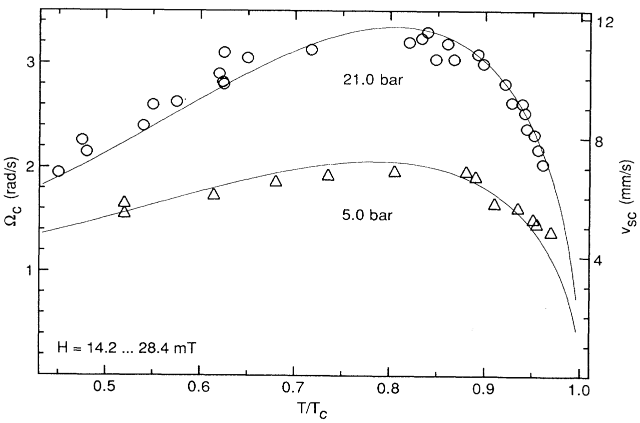

FIG. 3. Measurements on the critical rotation velocity Ω_c for the nucleation of singular B-phase vortices in the NMR cell of Fig. 2 in the vortex-free state, plotted as a function of normalized temperature. Nucleation takes place on the cylindrical side wall of the rotating container, thus Ω_c (left vertical axis) corresponds to a critical counterflow velocity $v_{sc}=\Omega_c R$ (right vertical axis). Measurements are shown at 21-bars (circles) and 5-bars (triangles) pressures. The solid curves represent $v_{sc}=c[1+\frac{1}{3}F_s^1 Y(T/T_c)]\Delta_B(T/T_c)/p_F$ (see Ref. 30). Here $c\sim 0.1$ is a constant factor. It represents the fraction by which the bulk liquid pair-breaking velocity is reduced by surface roughness, which catalyzes the nucleation of the singular-vortex core.

In the *equilibrium vortex state* the number of vortices is determined by minimization of the free energy in the rotating frame (see Sec. IV C). However, our measurements on the slow vortex mode relaxation have been performed at $\Omega<\Omega_c$ on a *metastable vortex cluster state,* where the number of vortices is less than the equilibrium number. The procedure for creating such a metastable vortex cluster with a known number of vortices is the following: First, Ω is rapidly accelerated to our maximum rotation velocity of about 3.5 rad/s. This is larger than Ω_c and an unspecified number of vortices is created. Next Ω is reduced to some lower value Ω_v so that some vortices are observed to annihilate. In uniform rotation at constant Ω the density of vortices is $n_v=2\Omega/\kappa$, where $\kappa=h/2m_3=6.65\times10^{-4}$ cm^2/s is the superfluid circulation. Thus, the deceleration to Ω_v adjusts the number of vortices to the value $N_v\approx 2\pi R^2\Omega_v/\kappa$. The final step is then to increase Ω again, whereby a vortex cluster is formed. The cluster is isolated by an annular vortex-free counterflow layer from the cylindrical cell wall (Fig. 4). During the increase in Ω the vortex number remains constant at $N_v=2\pi R_v^2\Omega/\kappa$, where $R_v=R\sqrt{\Omega_v/\Omega}$ is the diameter of the vortex cluster. This metastable vortex cluster state can now be examined at different Ω, within the limits $\Omega_v\leq\Omega<\Omega_c+\Omega_v$, without change in the number of vortices as long as the flow velocity at the cylindrical

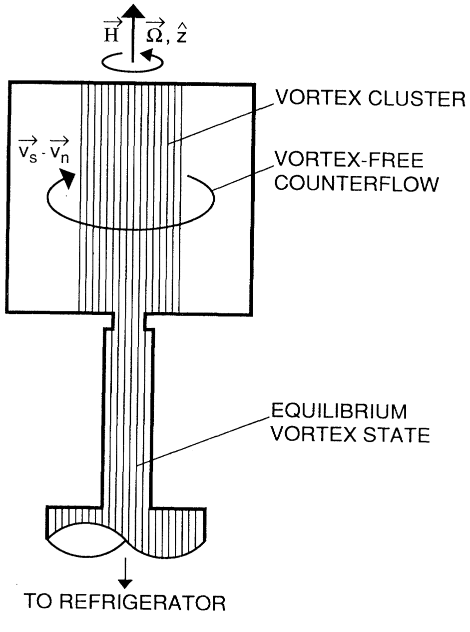

FIG. 4. NMR cell and the vortex cluster. The measurements on the slow vortex mode are performed in the metastable vortex cluster state: Here the vortices are contained inside a cluster in the center of the rotating container and are isolated by macroscopic vortex-free counterflow from the side wall. In this case the interaction between the peripheral vortices and the side wall is avoided. Also the rotation velocity can now be varied within the limits $\Omega_v\leq\Omega<\Omega_c(T,p)+\Omega_v$ and no vortices are annihilated or new ones nucleated.

wall $R(\Omega-\Omega_v)<R\Omega_c(T)=v_{sc}$.

Summarizing we note that vortex nucleation occurs in the NMR cell on the cylindrical container wall, independently of the size of the central vortex cluster, at $\Omega=\Omega_c(T)+\Omega_v$. The nucleation of a vortex takes place when the flow velocity exceeds a critical velocity. Due to surface roughness this critical velocity is reduced from the bulk pair-breaking value by a factor of ≈ 10. The nucleation process is associated with a high-energy barrier. In contrast, the annihilation process involves no essential barrier when the vortex is pushed back towards the wall during deceleration. These two situations do not involve the same phenomena and are therefore far from symmetric on the Ω axis.

After nucleation the vortex is pulled by the counterflow towards the center of the cell; this motion is driven by the Magnus force and damped by the mutual friction forces (Sec. V A). Both in the annihilation as well as in the nucleation process the bottleneck in the observed time dependence is the mutual-friction-resisted motion of the vortex, which occurs on a time scale of a few seconds and conceals the other faster processes.

IV. MEASURING TECHNIQUE

A. Homogeneously precessing domain (HPD)

The present NMR measurements have been performed using a particular resonance mode of ^{3}He-*B*, which is known as the homogeneously precessing domain.[15,29] In this dynamic spin domain the total nuclear spin magnetization $M\approx\chi_B H$, induced by the static polarization field **H**, precesses coherently with the transverse rf excitation field $\mathbf{H}_1(\omega_{\mathrm{rf}})$ with a tipping angle, which with respect to the direction of **H** is roughly 104°. In the continuous (cw) mode, the HPD can be maintained indefinitely in the arrangement shown in Fig. 5. Here a linear field gradient is superimposed on the static magnetic field **H** such that the total field increases towards the orifice of the NMR cell, i.e., $H(z)=H_0-z|\nabla H|$. A horizontal domain boundary separates the precessing domain (HPD) above the boundary from the nonprecessing domain below the boundary. The location $z=z_B$ of the boundary is defined by the condition that here the precession frequency, i.e., the rf frequency ω_{rf}, equals the Larmor frequency $\gamma H(z_B)$, where γ is the gyromagnetic ratio.

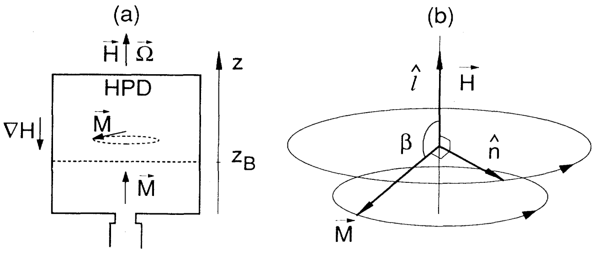

FIG. 5. (a) The NMR cell in the HPD measuring arrangement, with a magnetic field gradient ∇H and a large rf field transverse to **H**. The precessing domain (HPD) in the upper part is separated from the static domain in the lower part. (b) Orientation of the magnetization **M**, the axes $\hat{\mathbf{n}}$ and $\hat{l}=\mathbf{RM}/M$ in the HPD: $\hat{\mathbf{n}}$ is perpendicular to **H**, $\hat{l}$ is parallel to **H**, and **M** is tilted by the angle $\beta\approx104°$ in relation to **H** so that $\mathbf{M}\cdot\mathbf{H}\approx-\frac{1}{4}MH$ and $M\approx\chi_B H$.

The two-domain structure is supported by the interplay of the Zeeman and the dipole-dipole energies. In the static (nonprecessing) domain, where $H>\omega/\gamma$, the total free energy is minimized when $\mathbf{M}\|\mathbf{H}$. In the HPD, where $H<\omega/\gamma$, the free-energy minimization favors an **M** which is tilted in relation to **H** such that the tilting angle β is approximately equal to the value of the Leggett angle $\theta=\arccos(-\frac{1}{4})\approx104°$. In the HPD the torque from the dipole-dipole interaction compensates the torque from the Zeeman energy, so that uniform precession is possible in spite of ΔH. The *B*-phase order parameter includes the rotation matrix $\mathbf{R}(\hat{\mathbf{n}},\theta)$ which specifies a relative rotation of the orbital and spin coordinate systems around the axis $\hat{n}$ by the angle θ. In the HPD, the order parameter also participates in the precession: $\hat{n}$ precesses in the plane perpendicular to **H**, such that the orbital vector $\hat{l}=R\mathbf{M}/M$ is rotated to a stationary orientation along **H**.

When H is increasing towards the bottom of the NMR cell, then the HPD is first formed at the top of the cell. In this case no spin currents are leaking from the HPD and a more stable configuration is obtained than with ∇H oriented in the opposite direction. By sweeping H_0 one can change the volume of the HPD. For the absorption measurements it is advantageous to reduce H_0 so that the domain boundary is positioned at or just below the orifice. In this position the boundary and thus the relaxation from spin diffusion across the boundary are minimized. Also, any drift in the magnitude of the polarization field H has a minimal effect on the stability of the continuously monitored absorption level with the boundary at this location. These considerations on the stability of the HPD absorption provide one of the reasons for isolating the NMR cell with the epoxy plug from the rest of the tower. The second reason is to prevent the leakage of vortices from the lower parts of the chamber, as was explained in Sec. III.

As a result of the spin precession in the HPD, a strong signal is induced in the NMR pickup coil, which is proportional to the volume of the HPD while its phase is determined by the energy dissipation in the precession. Unlike in conventional NMR, the magnitude of $H_1(\omega_{\mathrm{rf}})$ does not influence the absolute value of the measured signal, but it is present in the phase difference between the signal and the rf field. These features have some consequences of technical nature, which are discussed below.

For sustaining the HPD mode, a large rf excitation field is required: in the setup of Fig. 2 a minimum field of $H_1>4\times10^{-4}$ mT is needed in order to compensate for the resonance absorption losses in the temperature range of our measurements. Conventional *B*-phase NMR spectra are recorded at an excitation level which is a factor of 10 or more lower. In the HPD mode the energy absorption $dE/dt\propto H_1M_\perp=\mathrm{const}$, where $M_\perp$ is the transverse part of the total spin component rotating in the xy plane and proportional to the absorption signal. For maximum resolution of the absorption signal it is useful to use a rf excitation which is as small as possible.

A reliable *in situ* temperature reading of the ^{3}He-NMR sample in the HPD mode is obtained by calibrating the amplitude of the measured cw resonance signal from the homogeneously precessing spins, when the domain fills the NMR cells. This signal is proportional to the component of the magnetization, which is precessing in the transverse plane, $\sqrt{M_\parallel^2+M_\perp^2} \propto \chi_B(T)H$, where $M_\parallel$ is proportional to the out-of-phase signal and $M_\perp$ to the in-phase signal at the lock-in amplifier output. The absolute value of the signal can be calibrated at some temperature below T_c, e.g., against the B-phase NMR frequency shifts, which are measured from a conventional NMR spectrum of the flare-out texture.[31] The temperature dependence of the B-phase susceptibility $\chi_B(T)$ has been measured in Ref. 32 and is used here to provide the temperature scale.

B. HPD resonance absorption measurement in the rotating state

A number of mechanisms contribute to magnetic dissipation in the HPD;[15] of interest to us are only those which appear in the rotating state when vortices are present. Counterflow and vortices both produce their characteristic signal behavior in the HPD resonance and can be distinguished from each other with good resolution.[33,16] Here we are only concerned with vortices. Localized inhomogeneities in the superfluid order-parameter field, such as a vortex core, are found to produce additional dissipation.[16] Since the cores are small compared to the intervortex distance, this absorption contribution is additive and can be used as a signal for monitoring the number of vortices. Furthermore, the magnitude of the additional absorption depends on the vortex core structure. In ^{3}He-B a first-order phase-transition line $T=T_v(p)$ separates vortices with two different singular core structures. At higher pressures and temperatures an axisymmetric vortex core is stable and exhibits small additional HPD absorption. At lower pressures and temperatures a nonaxisymmetric vortex core displays larger absorption. In addition, the absorption from the nonaxisymmetric vortices depends not only on their number, but also on their motional state, i.e., whether they are stationary or in translational motion. The latter feature is crucial for the existence of the HPD signal from the slow vortex mode, which is observed only in the case of the nonaxisymmetric vortices. It will be discussed in Sec. IV E.

In all of the present measurements the static polarization field is oriented axially ($\mathbf{H}\parallel\mathbf{\Omega}$), which maximizes the HPD absorption losses from vortices and is, moreover, the only useful orientation of the field for the measurement of the slow mode signal (see Sec. IV E). Most of the present HPD absorption measurements have been performed at $\omega_{\mathrm{rf}}/(2\pi)=460$ kHz (which corresponds to $H=14.2$ mT), where the amplitude resolution in the measurement of the slow mode signal is best.[16] In Fig. 6, an example of the cw HPD resonance absorption signal at the lock-in output is displayed as a function of time, while the rotation velocity is reduced in a steplike manner. The total reduction in the rotation-dependent absorption from the initial state at 0.59 rad/s to the final state at 0.44 rad/s is a 7-μV drop in the rf voltage of 12 mV across the tank circuit, which here has a Q-value of 54. The voltage drop translates to an 8-pW absorption loss[34] and corresponds to the annihilation of ≈ 170 vortices. With a lock-in amplifier time constant of 0.1 s, the peak-to-peak noise of the recorder trace corresponds to ≈ 14 vortices.

The present experimental results are extracted from the Ω-dependent HPD absorption signal; its time-dependent properties are illustrated in Fig. 6. In the starting situation the rotating container is filled here with an equilibrium number of vortices $N_v \approx 2\pi R^2\Omega_i/\kappa$ at the initial rotation velocity $\Omega_i=0.59$ rad/s and the absorption level is constant. When Ω is reduced in a linear sweep, the absorption signal displays a time-dependent transient and then settles to a new stable level, which corresponds to the equilibrium state at $\Omega_f=0.44$ rad/s and $N_v \approx 2\pi R^2\Omega_f/\kappa$. The transient displays as a function of time three different processes, which we interpret as fol-

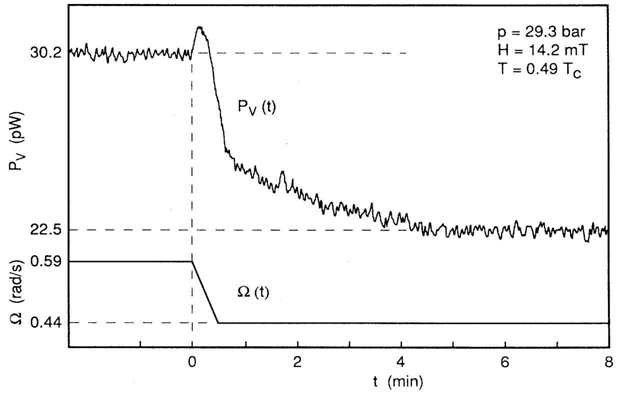

FIG. 6. Response of the cw HPD resonance absorption level P_v to a reduction in Ω. The measurement is performed on the nonaxisymmetric ^{3}He-B vortices with $\mathbf{H}\parallel\mathbf{\Omega}$. Both the initial and final states are equilibrium vortex states with the maximum number of vortices at these Ω values, i.e., there is no macroscopic counterflow. P_v (upper trace) is here recorded as a function of time t, while Ω (lower trace) is reduced from the initial state at 0.59 rad/s to the final state at 0.44 rad/s. This reduction corresponds to the annihilation of ≈ 170 vortices. With a signal averaging time of 0.1 s the peak-to-peak noise of the recorder trace corresponds to ≈ 14 vortices. The absorption response $P_v(t)$ goes through three stages which are interpreted as follows: (1) The initial increase immediately after $t=0$ is a characteristic of the HPD absorption mechanism of the nonaxisymmetric vortices when they are forced into motion (see Appendix A). (2) The increase is soon eliminated by a rapid drop in the signal level during the next 30 s, which is caused by the annihilation of the excess vortices at the cylindrical wall of the NMR cell. The time dependence here is dictated by the mutual-friction-resisted motion of these vortices and by the rate of deceleration of Ω (a choice of a more rapid deceleration would have obliterated the initial absorption maximum). (3) The final slowly varying signal response, extending over several minutes, is an exponential relaxation. Here the time dependence is governed by the slow mode while the HPD absorption amplitude is controlled by the same dissipation mechanism as during the initial increase [(1) above].

lows.

(1) Rapid initial increase after switching on the deceleration of Ω, which sets the nonaxisymmetric vortices into motion: The HPD absorption increase here is caused by the same mechanism which is responsible for the signal amplitude during the slow mode [see (3) below]. The increase takes place during the time-dependent Ω drive which forces the vortex motion. (Forced vortex motion is discussed in Appendix B.)

(2) Rapid decrease. The second process is a rapid decrease in signal level. The time dependence here is a characteristic of the fast mutual-friction-resisted mode (Sec. VI), while the amplitude is governed by the annihilation of the excess vortices at the cylindrical container wall.

(3) Exponential relaxing tail. The final process represents the slow vortex mode (Sec. VII). The signal amplitude is here governed by a dissipation mechanism of the nonaxisymmetric vortices; its discussion is postponed to Appendix A.

Summarizing, we note that the analysis in this paper is concentrated on the time dependence of the decreasing part of the signal in Fig. 6. It consists of two distinct phases (as was schematically shown in Fig. 1): the initial fast motion and the slow asymptotic phase at long times. These can be isolated from each other by simple experimental procedures and can thus be analyzed separately. This analysis will be discussed in Secs. IV D and IV E.

C. Measurement of the number of vortices

The HPD resonance absorption contribution P_v from vortices has been found to be proportional to the number of vortices N_v within the precessing domain, which is given by $N_v = \pi R_v^2 \Omega/\kappa$ for a metastable vortex cluster.[16] In Fig. 7, the Ω-dependent component P_v in the HPD absorption level has been plotted for equilibrium vortex states as a function of Ω. These equilibrium vortex states have been created by first accelerating the cryostat rapidly to 3.5 rad/s, which exceeds the critical rotation velocity Ω_c for nucleating vortices and essentially fills the NMR cell with vortices. Next Ω is reduced to some value where P_v starts to decrease, which is a sign for the fact that the NMR cell is completely filled with vortices and a further reduction in Ω causes the surplus of vortices to move to the wall and to be annihilated. Now the data collection for Fig. 7 is started by reducing Ω stepwise and by recording the corresponding reductions in the equilibrium value of $P_v(\Omega)$. Figure 6 is an example of such a recording following a rapid reduction of Ω by $\Delta\Omega$.

At low rotation velocities the plot in Fig. 7 deviates from the dependence $P_v \propto \Omega$, which would correspond to a horizontal line in the plot. The following considerations should be noted in this context.

(1) Remnant vortices. Deceleration to a lower Ω value may not necessarily lead to the equilibrium vortex number, i.e., the final state could deviate from the minimum energy state. A small surplus of remnant vortices may be left behind which are not annihilated at the wall. There are no indications for the presence of remnant vortices in our ^{3}He-NMR cell within our resolution of ±10 vortices [21] while for superfluid ^{4}He this has been reported from numerous experiments of different kinds.[20,35]

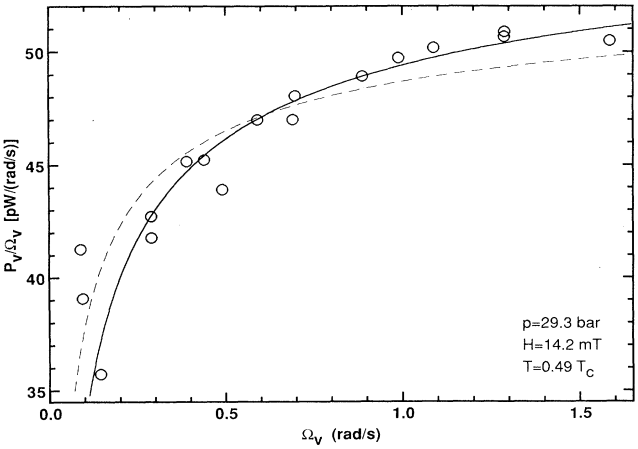

FIG. 7. Measurement of the number of vortices in the NMR cell as a function of Ω. The HPD resonance absorption contribution P_v from vortices has been plotted in the normalized form P_v/Ω as a function of Ω in the equilibrium state ($\Omega = \Omega_v$). Here the cryostat is decelerated in a steplike fashion from one equilibrium vortex state to the next, as shown in Fig. 6, and P_v monitors the change in the number of vortices. (The two stable absorption levels at 0.59 and 0.44 rad/s in Fig. 6 are among the data points in this figure.) The two curves represent fits to Eq. (4.2): solid curve (best fit to P_v vs Ω), $P_v/\Omega = 57.8(1-\sqrt{0.0056/\Omega})^2$ pW; dashed curve (best fit to P_v/Ω vs Ω), $P_v/\Omega = 54.2(1-\sqrt{0.0027/\Omega})^2$ pW. In this plot the deviation from a constant P_v/Ω value at low Ω emphasizes the influence from the vortex-free region. Here the measurement is performed at low temperatures on nonaxisymmetric vortices. It can also be performed at high temperatures on axisymmetric vortices, but with poorer resolution because of their smaller P_v.

(2) Suppression of the HPD absorption signal by the wall interaction. This effect is discussed in Appendix B 3. It depends strongly on the distance of the outermost vortices from the wall and applies only to the nonaxisymmetric vortices. At small rotation velocities, i.e., at large intervortex distances, where the relative deviation from the dependence $P_v(\Omega) \propto \Omega$ is largest, this effect is not important.

(3) Vortex-free region. Even in the equilibrium state a narrow annular vortex-free layer isolates the vortices from the container wall.[27] We shall analyze Fig. 7 in terms of this phenomenon.

The width of the vortex-free region is given by[27,36]

$$d = \left[\frac{\kappa}{4\pi\Omega} \ln \frac{r_v}{r_c} \right]^{1/2} , \tag{4.1}$$

which is roughly equal to one intervortex distance $\sqrt{\kappa/(\sqrt{3}\Omega)}$ in ^{3}He-B and between one and two intervortex distances in ^{4}He. For convenience here we simply set $r_v = \sqrt{\kappa/(\sqrt{3}\Omega)}$, while r_c is a measure of the vortex-core radius. Because of the vortex-free region, the strict proportionality $N_v \propto \Omega$ is not obeyed in the equilibrium state. The equilibrium number of vortices then becomes

$$N_v = \frac{2\pi\Omega(R-d)^2}{\kappa} = \frac{2\pi\Omega R^2}{\kappa}\left[1-\left[\frac{\kappa}{4\pi\Omega R^2}\ln(r_v/r_c)\right]^{1/2}\right]^2 . \qquad (4.2)$$

This result, which is derived for the continuum limit, is well obeyed even at small vortex numbers $N_v < 100$, as has been shown by numerical simulations.[37] Roughly speaking, these studies in superfluid ^{4}He have shown that the effect of the wall is to suppress the formation of one outermost ring of vortices.

In Fig. 7, our measurements on the number of vortices as a function of Ω have been plotted in the normalized form with P_v/Ω on the vertical axis. In the fitting process we have neglected the Ω dependence from the term $\ln(r_v/r_c)$ and have used a formula $P_V(\Omega) = P_0\Omega(1-\sqrt{\Omega^*/\Omega})^2$ with the fitting parameters P_0 and Ω^*. Two fits are shown which give $\Omega^* = 5.6\times10^{-3}$ rad/s (solid curve) and $\Omega^* = 2.7\times10^{-3}$ rad/s (dashed curve), which exemplifies the precision with which the vortex-free region can be resolved from the measurements. The expected value in Eq. (4.2) is

$$\Omega^* = \kappa/(4\pi R^2)\ln(r_v/r_c) \approx 3\times10^{-3} \text{ rad/s} .$$

From this comparison displayed in Fig. 7 it follows that one can count the number of vortices corresponding to any value of Ω_v. At present our resolution is limited in this measurement to ±20 vortices.

D. Measurement of the fast motion

In the first rapidly decreasing part of the HPD absorption response in Fig. 6, the amplitude of the signal $P_v(t)$ monitors the number of vortices $N_v(t)$ in the NMR cell, while the vortex cluster expands and the excess vortices annihilate at the wall. The time scale of this process is dominated by the motion of the vortices to the wall and not by their annihilation. Thus, the time dependence can be exploited for extracting the mutual friction (Sec. VI).

The fast mutual-friction-resisted relaxation is most effectively displayed and measured by suddenly stopping rotation from a high initial Ω with a large number of vortices and by then recording the evolution of $N_v(t)$ while all the vortices move to the wall and annihilate. The measurement is illustrated in Fig. 8. In this case the final state is the $\Omega=0$ state with no vortices and the tail of the fast relaxation signal, which is of the form $N_v \propto 1/(1+t/\tau_F)$, is not masked by the slow relaxation, as is the case of Fig. 6.

E. Measurement of the slow vortex mode

The HPD signal from the slow mode is a characteristic of the nonaxisymmetric *B*-phase vortex. The amplitude of the slowly relaxing signal response $\Delta P_v(t)$ in Fig. 6 is also $\propto N_v$, but this process takes place while N_v is already essentially constant. Thus, the absorption mechanism here is different. It is discussed in Appendix A. Our measurements on the slowly relaxing signal have been performed on vortex clusters which are isolated from the cylindrical container wall by a wide vortex-free region, as shown in Fig. 4. If the cluster is not in contact with the wall at any time during the measurement, then the number of vortices is maintained unchanged and also any interaction of the outermost vortices with the wall is avoided.

A simple and reproducible procedure for exciting the slow relaxation response with a *harmonic hydrodynamic drive* is illustrated in Fig. 9. Here a harmonically varying component is superimposed on the steady rotation drive at $\Omega_0 = 1.5$ rad/s, such that the rotation velocity becomes $\Omega(t) = \Omega_0 + \Delta\Omega(1-\cos\omega_m t)$. The modulation frequency is $\omega_m/(2\pi) = 1/30$ s^{-1} and its amplitude $\Delta\Omega = 0.05$ rad/s. The modulation is switched off when a new steady absorption level is reached and then the relaxation back to the initial state with $\Omega(t) = \Omega_0$ is monitored. After stopping the Ω modulation, the vortex density first rapidly adjusts by the fast mutual-friction-resisted motion close to its equilibrium value. This process is only implicitly present in the response in Fig. 9 as a brief initial nonexponential phase of the relaxation decay and we may neglect it completely. The slow decay of $\Delta P_v(t)$ in Fig. 9 can then be fitted with one exponential time constant τ_s which is 2 orders of magnitude slower than the time scale

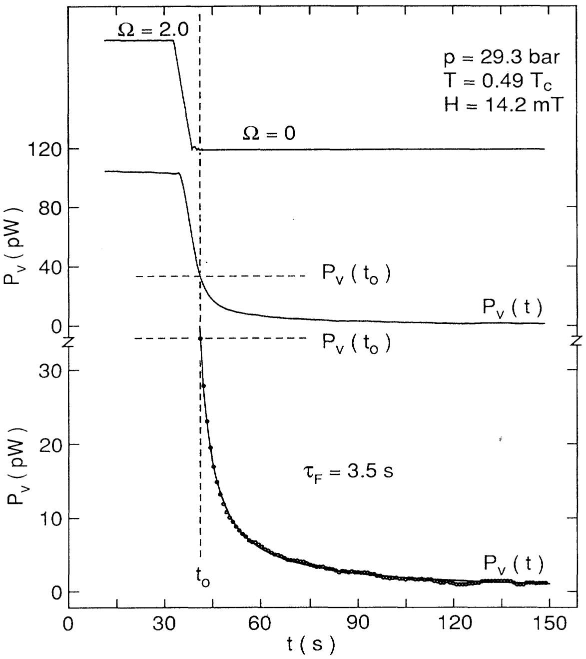

FIG. 8. Measurement of the fast mutual-friction-resisted motion after stopping the rotation: $\Omega(t)$ and $P_v(t)$ are plotted as a function of time during a rapid linear deceleration of Ω from 2.0 rad/s to a total stop. The rapidly relaxing signal is plotted in the middle on a coarse amplitude scale showing the complete time response and on the bottom on a five times amplified scale, which illustrates the final phase of the signal decay, after the cryostat has been brought to a complete stop. This part of the signal decay at $t > t_0$ has been fit to Eq. (6.5), which gives for the characteristic decay time $\tau_F = 3.5$ s. Here the solid curve represents the fit while the data points are from the trace shown in the middle.

τ_F of the fast mutual-friction-resisted motion.

The slow signal is thus obtained while the vortex density is already close to its final equilibrium value, but the positions of individual vortices still deviate from those in the final equilibrium state. The time dependence of the exponentially relaxing signal, which is here observed in the absence of any external perturbations, we associate with the slowest collective mode of the vortex array, i.e., the mode which is responsible for the asymptotic exponentially slow approach to the equilibrium configuration. We call it the *slow vortex mode.* In contrast, the first transient part of the response in Fig. 9 following the switch on of the Ω modulation is a sum of both the fast and slow modes and will not be analyzed here in detail. The steady-state motion during the harmonic rotation drive, which corresponds to the stable maximum signal level in Fig. 9, is analyzed in Appendix B.

Figure 9 shows that the resonance amplitude $\Delta P_v(t)$ is associated with hydrodynamic motion: It appears when the vortices are forced into translational motion and it disappears exponentially when the vortices settle down to their pinned equilibrium sites. Another example of the coupling of $\Delta P_v(t)$ at constant vortex number to the hydrodynamics is the interaction of the peripheral vortices with the cylindrical container wall and its dependence on the distance from the wall, which is discussed in Appendix B.

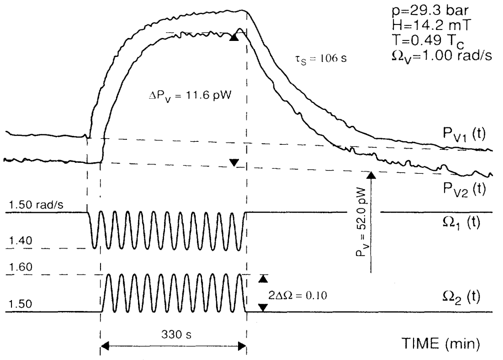

FIG. 9. Measurement of the slow vortex mode. P_v is monitored as a function of time while a sinusoidal component is either subtracted from [trace $\Omega_1(t)$] or added to [trace $\Omega_2(t)$] the constant rotation $\Omega_0 = 1.5$ rad/s. The measurement is performed on a vortex cluster, whose equilibrium state is at $\Omega_v = 1.0$ rad/s (i.e., at Ω_v the cluster fills the whole NMR cell). The responses $P_{v1}(t)$ and $P_{v2}(t)$ to the two drives $\Omega_1(t)$ and $\Omega_2(t)$ are identical; the absorption increase ΔP_v does not depend on whether the cluster starts to contract or expand and is thus a function of only the modulus of vortex displacement. The harmonic component in the drive enforces a relative change in vortex density, which is $\propto \Delta\Omega/\Omega_0 \approx 7\%$ peak to peak. When the harmonic component in the drive is switched off, the signal decay to the final state at Ω_0 is, for the most part, controlled by the slow vortex mode, since $\tau_s \gg \tau_F$. This exponential relaxation of $\Delta P_v(t)$ is fitted with a time constant $\tau_s = 106$ s, equal for both responses; the quality of the fit depends primarily on the stability of the base line for the absorption increase ΔP_v (dashed horizontal lines). Here the base lines have a finite slope due to a slow drift in the electronics.

In addition to the hydrodynamic drive, the slow mode can be excited by any means which disturb momentarily the equilibrium state. A short transient perturbation is, e.g., a thermal pulse, which is introduced by overheating the Pt NMR coil with a number of large transmitter pulses. The thermal pulse is accompanied by a hydrodynamic disturbance since it involves some redistribution of the angular momentum. A temperature transient changes the ratio of the normal and superfluid components and, as a result, an exchange of angular momentum takes place between them. Similarly, a magnetic disturbance can be used to excite the slow mode. This can be effected by simply switching on the HPD, i.e., by sweeping the steady field H down, such that the HPD is formed. On the other hand, if this operation is performed by starting from an existing HPD, i.e., by sweeping the field first up, such that the HPD is removed, and then after a time interval Δt back down again, the signal amplitude is a function of Δt: if the time Δt is small compared to the time τ_s, the interruption of the HPD has no effect on the signal, it returns back to the former level before the interruption (two operations in rapid succession cancel each other). When $\Delta t \gg \tau_s$, the signal becomes independent of when the former HPD was switched off.

When $\mathbf{H}$ is tilted beyond a critical inclination angle η_c with respect to the rotation axis $\boldsymbol{\Omega}$ (at $H = 14.2$ mT, $\eta_c = 17°$), neither hydrodynamic, thermal, nor magnetic drives are observed to excite any changes in the HPD absorption level. This excludes a thermal process as a possible explanation of the slow relaxation. On the other hand, the tilted magnetic field suppresses the absorption mechanism, suggested by us for the exponentially relaxing signal $\Delta P_v(t)$ (see Ref. 16 and Appendix A).

From the measurements of the exponential relaxation we have found that τ_s does not depend on the perturbation, which is used to initiate the slow mode, but instead it is controlled by the hydrodynamic conditions. Nor does τ_s appear to depend on the tilting angle η in the range $0 \le \eta < \eta_c$ where the relevant absorption mechanism is present or on the fact whether the vortex cluster is in contact with the cylindrical cell wall or not. Also, as seen from Fig. 9, the slow response is insensitive to whether the change in Ω corresponds to acceleration or deceleration: In fact, a stepwise increase or decrease in Ω, acting on a vortex cluster isolated by macroscopic counterflow from the cell wall, produces identical responses.

The chain of mechanisms, which connects the slow vortex mode to the HPD absorption, is not yet clear in all details (see Appendix A). However, this is not of primary concern to us here since we study the time dependences, which are governed by hydrodynamics. Among the several reasons, which dictate a close connection between the measured exponential relaxation of $\Delta P_v(t)$ and the hydrodynamic slow mode, the most compelling argument is the long time scale of $\tau_s \sim 100$ s: no other process at constant temperature has a time scale relevant to the observed time variations. Magnetic relaxation phenomena are all at least 4 orders of magnitude faster, i.e., a few ms or faster. Also, the readjustment of the vortex array to a new equilibrium vortex density is 2 orders of magnitude faster. We therefore believe that the time dependence in the exponentially relaxing part of the absorption signal is of hydrodynamic origin and is caused by the slow vortex mode, since asymptotically at large time scales only the slowest mode survives and is expected to display exponential time dependence. From the experimental point of view it is fortunate that the time scale of the slow mode is well separated from that of any other relevant mode. The remaining part of the main text of the paper is devoted to an analysis of hydrodynamic motion, which is then compared to the present experimental results.

V. SUPERFLUID VORTEX DYNAMICS: GENERAL PRINCIPLES

A. Equation of motion: Mutual friction

As already known from the 19th century, the motion of a single vortex in a classical incompressible perfect fluid is governed by the dynamic equation

$$\kappa\rho[\hat{\mathbf{z}}\times(\mathbf{v}_L-\mathbf{v})]=\mathbf{f}\ . \qquad (5.1)$$

Here the vortex line is taken to be parallel to the z axis, $\mathbf{v}_L$ is the velocity of the vortex line in the xy plane, $\mathbf{v}$ is the velocity of fluid flowing past the vortex line, ρ is the fluid mass density, κ is the circulation around the vortex, and $\mathbf{f}$ is the transverse external force per unit length acting on the vortex line. If there is no external force, the vortex moves with the fluid velocity: $\mathbf{v}_L=\mathbf{v}$ (Helmholtz theorem). Equation (5.1) shows that an external force acting on a vortex is balanced not by the inertial force proportional to acceleration as in Newton's second law for the motion of a particle, but by the Magnus force proportional to the velocity of the vortex in the frame moving with the fluid.

According to the two-fluid hydrodynamics of superfluids, only the superfluid component is a perfect inviscid fluid and superfluid vortices are singular lines in the superfluid velocity field $\mathbf{v}_s$. This means that the density ρ and the velocity $\mathbf{v}$ in Eq. (5.1) should be replaced by the superfluid density ρ_s and the superfluid velocity $\mathbf{v}_s$. On the other hand, the vortex interacts with excitations or quasiparticles in the normal component of the fluid; this interaction gives rise to the mutual-friction force $\mathbf{f}_{ns}$ which plays the role of the external force $\mathbf{f}$ in Eq. (5.1). So one can write the equation of superfluid vortex motion as

$$\kappa\rho_s[\hat{\mathbf{z}}\times(\mathbf{v}_L-\mathbf{v}_s)]=\mathbf{f}_{ns}\ . \qquad (5.2)$$

The mutual friction force per unit length of the vortex line is proportional to the relative velocity of the superfluid and the normal components (i.e., the counterflow $\mathbf{v}_s-\mathbf{v}_n$) and is generally expressed in the Hall-Vinen form[38]

$$\mathbf{f}_{ns}=-\frac{\kappa\rho_s\rho_n}{2\rho}\{B\hat{\mathbf{z}}\times[\hat{\mathbf{z}}\times(\mathbf{v}_s-\mathbf{v}_n)]+B'[\hat{\mathbf{z}}\times(\mathbf{v}_s-\mathbf{v}_n)]\}\ , \qquad (5.3)$$

which is written in terms of a dissipative component parallel to the counterflow $\mathbf{v}_s-\mathbf{v}_n$ with the coefficient B and a reactive perpendicular component with the coefficient B'. From Eqs. (5.2) and (5.3) one obtains the basic equation governing the motion of a vortex line in the two-fluid hydrodynamics:

$$\mathbf{v}_L=\mathbf{v}_s-B\frac{\rho_n}{2\rho}[\hat{\mathbf{z}}\times(\mathbf{v}_s-\mathbf{v}_n)]-B'\frac{\rho_n}{2\rho}(\mathbf{v}_s-\mathbf{v}_n)\ . \qquad (5.4)$$

In superfluid ^{3}He at any experimentally practical frequencies the normal component can be considered to be clamped to corotation with the container. In a step change of Ω the normal component adjusts to the new rotation velocity exponentially with the time constant of a classical viscous fluid $\tau_n=(R/3.83)^2/\nu\leq 10$ ms (where $R=0.35$ cm is the radius of our NMR cell, 3.83 is the first zero of the Bessel function $J_1(x)$, and ν is the kinematic viscosity of the normal component).[39] This is 2 orders of magnitude faster than the fastest times characterizing the experimentally observed vortex motions in superfluid ^{3}He. Therefore, the normal component is clamped to corotation with the container, as is assumed throughout this paper; then in the frame rotating with the container $\mathbf{v}_n=0$ and the vortex moves with the velocity

$$\mathbf{v}_L=\left[1-B'\frac{\rho_n}{2\rho}\right]\mathbf{v}_s-B\frac{\rho_n}{2\rho}[\hat{\mathbf{z}}\times\mathbf{v}_s]\ . \qquad (5.5)$$

Equations (5.2)–(5.5) are derived for a single straight vortex line, but remain valid also for a deformed vortex or a system of deformed vortices even if the deformations are rather strong, as in the Berkeley experiment on the precession of a single vortex in superfluid ^{3}He-B.[40] Then $\mathbf{v}_s$ and $\mathbf{v}_n$ are velocities in the vicinity of an element of the vortex line moving with the velocity $\mathbf{v}_L$, all three velocities lying in the plane normal to the element of the vortex line. The only conditions restricting their applicability are (i) the radius of curvature of the vortex line must be much larger than the vortex core radius r_c and (ii) the distance between vortex lines must be much larger than r_c. The superfluid velocity $\mathbf{v}_s$ includes the velocity field induced by all other vortex lines as well as by other elements of a given deformed vortex line. Thus, all collective effects due to long-range interaction of vortices are present in the superfluid velocity $\mathbf{v}_s$. Later we shall see how the vortex interaction manifests itself in the superfluid velocity field.

In the pioneering work by Hall and Vinen,[38] the mutual friction force was considered to arise from the scattering of noninteracting quasiparticles by vortices (for a review of later progress see Refs. 1, 11, 13, and 41). Because of broken time invariance (clockwise and counterclockwise rotations are not equivalent due to the presence of circulation), the scattering leads not only to a dissipative force $\propto B$, but also to a reactive force $\propto B'$ [see Eq. (5.3)]. Since there are no quasiparticles at $T=0$, the parameters B and B' should approach zero when the temperature decreases to zero. The problem with the theory of mutual friction in the regime of noninteracting quasiparticles in both ^{3}He and ^{4}He is that it predicts values of B much smaller than is obtained from experiment. Mutual friction of singular vortices in superfluid ^{3}He has recently been discussed by Kopnin and Salomaa.[42] They found that at low temperatures, including the region of the present measurements around $0.5T_c$, the dominant contribution arises from the mutual interaction between the bulk quasiparticles and quasiparticles localized in the singular vortex core. The estimated value of B from the bound-state contribution in the core was found to be in qualitative agreement with experiment. At the same time the value of B' turned out to be comparatively small.

At increasing T the approach based on the scattering theory of noninteracting bulk quasiparticles becomes invalid since the mean free path of the quasiparticles becomes shorter than the relevant length scale, on which the scattering from the core occurs. Close to T_c another approach to mutual friction may be used: the hydrodynamic equations for the normal component are solved together with the time-dependent Ginzburg-Landau equations for the order parameter (see discussion for superconductors in Ref. 43). In ^{4}He, the renormalized Ginzburg-Pitaevskii theory (the analog of the Ginzburg-Landau theory) (Ref. 44) has been used to perform this analysis.[45] This approach is justified if the radius of the vortex core exceeds the mean-free-path length of quasiparticles. It is worth noting that mutual friction for the large continuous vortices in ^{3}He-A (Ref. 46) may be treated purely within the hydrodynamic approach at any temperature.[47]

The dissipative mutual friction $B\rho_n/\rho$ can be extracted from the analysis of the measured fast relaxation signal (Sec. VII); the result is displayed in Fig. 10. The line through the measured data extrapolates smoothly to earlier measurements, performed at 20 bars close to T_c.[48] The latter measurements, in which the dissipation of oscillatory superflow was studied in the rotating state, showed that $B\rho_n/\rho$ increases steeply from 4.9 at $0.88T_c$ to 8.7 at $0.97T_c$.

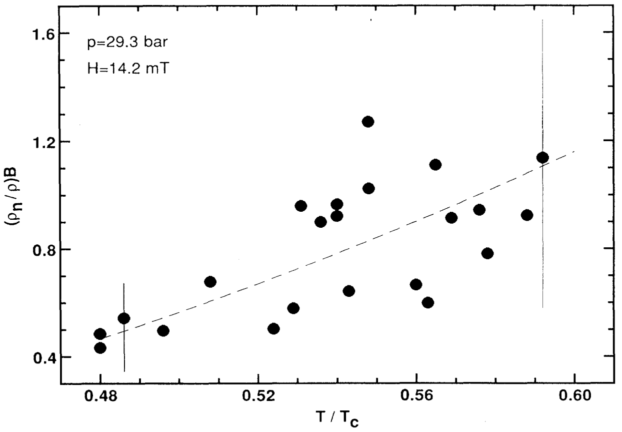

FIG. 10. Measured temperature dependence of the dissipative mutual friction coefficient $B\rho_n/\rho$. The data points have been extracted from the measurements of the fast mutual-friction-resisted decay time τ_F of the nonaxisymmetric vortex at 29.3 bars (see Sec. VI): the relation $B\rho_n/\rho=(\tau_F\Omega_0)^{-1}$ is used, where Ω_0 corresponds to the number of vortices $N_v(t_0)=2\pi R^2\Omega_0/\kappa$ at $t=t_0$ from where the fit to the measured signal decay is started, as indicated in Fig. 8. The dashed curve represents a smooth average through the present data and those of Ref. 48, measured at 20 bars and high temperatures $0.88\le T/T_c\le 0.97$.

B. Collective effects: Columnar motion

In order to complete the system of equations describing the motion of vortex lines, one needs an equation connecting the superfluid velocity $\mathbf{v}_s$ and the vortex velocity $\mathbf{v}_L$. This is the Euler equation, which can be written in the coordinate frame rotating with an arbitrary constant angular velocity Ω as[13]

$$\frac{d\mathbf{v}_s}{dt}+[2\mathbf{\Omega}_s\times\mathbf{v}_L]=-\nabla\left[\mu+\frac{v_s^2}{2}\right] . \tag{5.6}$$

Here

$$\mathbf{\Omega}_s=\mathbf{\Omega}+[\nabla\times\mathbf{v}_s]/2 \tag{5.7}$$

is the superfluid vorticity in the laboratory frame and μ is the chemical potential. The superfluid is taken to be incompressible: $\nabla\cdot\mathbf{v}_s=0$. The linearized version of Eq. (5.6) ($\mathbf{\Omega}_s=\mathbf{\Omega}$) is

$$\frac{d\mathbf{v}_s}{dt}+[2\mathbf{\Omega}\times\mathbf{v}_L]=-\nabla\mu . \tag{5.8}$$

Equations (5.6) or (5.8) account for the collective effects: the velocity field $\mathbf{v}_s$ is induced by other vortices.

Let us consider the implications from collective effects in a simple case in the absence of mutual friction, when $\mathbf{v}_L=\mathbf{v}_s$ in Eq. (5.8), namely, the inertial wave as an illustration of columnar motion of the fluid. This wave was well-known in the hydrodynamics of rotating classical fluids.[49] In columnar motion, flow is restricted to the transverse plane and any component along $\hat{\mathbf{z}}$ is uniform. We look for a solution in the form of a plane wave $\propto\exp(ipz+i\mathbf{q}\cdot\mathbf{r}-i\omega t)$, with p and $\mathbf{q}$ being the components of the wave vector along the z axis and in the xy plane, respectively. Here $\mathbf{r}$ is the position vector in the xy plane. Introducing the components $(v_s)_z$, $(v_s)_q$, and $(v_s)_t$ of $\mathbf{v}_s$ along $\hat{\mathbf{z}}$, $\mathbf{q}$, and the axis normal to both $\hat{\mathbf{z}}$ and $\mathbf{q}$, one can rewrite Eq. (5.8) (note that $\mathbf{v}_L=\mathbf{v}_s$ now) in the Fourier representation for these components:

$$\begin{aligned}&-i\omega(v_s)_z=-ip\delta\mu ,\\&-i\omega(v_s)_q-2\Omega(v_s)_t=-iq\delta\mu ,\\&-i\omega(v_s)_t+2\Omega(v_s)_q=0 .\end{aligned} \tag{5.9}$$

Here $\delta\mu$ is the variation of μ induced by the wave. Excluding $(v_s)_z$ and $\delta\mu$ from these equations with the help of the incompressibility condition $\nabla\cdot\mathbf{v}_s=ip(v_s)_z+iq(v_s)_q=0$, one obtains a system of equations for the in-plane components:

$$\begin{aligned}&-i\omega(v_s)_q-2\Omega(v_s)_t\frac{p^2}{p^2+q^2}=0 ,\\&-i\omega(v_s)_t+2\Omega(v_s)_q=0 .\end{aligned} \tag{5.10}$$

The solution of these equations yields the spectrum of the inertial wave:[49]

$$\omega^2=4\Omega^2\frac{p^2}{p^2+q^2} . \tag{5.11}$$

This spectrum illustrates the Taylor-Proudman theorem: The slow motion of the rotating fluid ($\omega \ll \Omega$) is always columnar, i.e., $p \ll q$ and the velocity varies weakly along the z axis so that the vortex lines remain straight. This is the simplest illustration on how columnar motion of vortex lines arises due to collective effects in a vortex array. The concept of columnar motion is of utmost importance in the analysis of the slow vortex motions.

In the inertial wave motion the ratio of the in-plane velocity components is according to Eq. (5.10):

$$\frac{(v_s)_q}{(v_s)_t}=\frac{i\omega}{2\Omega}=\frac{\pm ip}{\sqrt{p^2+q^2}} . \tag{5.12}$$

Thus, the polarization of the inertial wave varies from linear for in-plane propagation ($p=0$) to circular for axial propagation ($q=0$). The spectrum of the inertial wave is strongly anisotropic and singular in the limit $p,q \rightarrow 0$. If the wave vector does not belong to the plane normal to the rotation axis ($p \neq 0$), the frequency is finite. A finite frequency (i.e., the existence of a gap in the oscillation spectrum) represents the collective effect from the long-range interaction of vortices and is similar to the gap in the oscillation spectrum of a plasma due to the long-range Coulomb interaction. For the collective effects under discussion quantization of circulation in quantum fluids is not relevant, since they are determined only by the circulation density $\nabla\times\mathbf{v}_s$ (which is exactly equal to 2Ω) and are preserved in the classical limit, when the circulation quantum $\kappa \rightarrow 0$.[13,50]

Both the fast (Sec. VI) and slow (Sec. VII) vortex modes involve columnar motion of rectilinear vortex lines, which is restricted to the xy plane. Mutual friction provides the damping in the inertial wave; in the next section mutual friction is incorporated in the analysis when we discuss the fast mutual-friction-resisted mode.

VI. FAST MUTUAL-FRICTION-RESISTED MOTION

The fast mutual-friction-resisted mode is responsible for the readjustment in vortex density of the rectilinear vortex lines in an expanding or contracting vortex cluster. This mode is displayed in the fast initial decay of the HPD absorptions signal in Fig. 6. Here the motion of the vortex lines is impeded by the drag from mutual friction while the driving force is produced by the vortex density attempting to achieve equilibrium with the momentary rotation velocity Ω.

The mutual-friction-resisted mode of a vortex array has been worked out in Ref. 51. It has also been applied to a measurement[52] of continuous vortices in the A phase in a "rapid stop experiment," similar to the one illustrated in Fig. 8. In the A phase each continuous vortex, which lacks a singular hard core, contributes an equal absorption increment to an absorption line which is known as the vortex satellite line and is shifted from the bulk A liquid cw NMR line. However, compared to the HPD resonance measurement of vortices in the B phase, the resolution is poorer in the measurement of the A-phase vortex number.

In order to describe the rearrangement in vortex density, when the initial state is far from equilibrium, we refer to the nonlinear Euler equation (5.6). Vortex lines are assumed to remain strictly rectilinear during their motion; thus, there is no motion along $\hat{\mathbf{z}}\|\mathbf{\Omega}$. This allows us to assume that the velocity $\mathbf{v}_s$ close to the vortex line, which enters Eq. (5.5), does not differ from that in Eq. (5.6), when averaged over the unit cell of the vortex array.

On taking the rotor of Eq. (5.6), one obtains the continuity equation for vortices:

$$\frac{d\Omega_s}{dt}+\nabla\cdot(\Omega_s\mathbf{v}_L)=0 , \tag{6.1}$$

or, assuming that the vortex cluster remains spatially homogeneous,

$$\frac{d\Omega_s}{dt}+\Omega_s(\nabla\cdot\mathbf{v}_L)=0 . \tag{6.2}$$

Remember that the normal component is assumed to maintain the solid body velocity $v_n(r)=\Omega r$. We use a frame fixed to the rotating vessel, where $\mathbf{v}_n$ is taken to vanish. There one can exclude $\mathbf{v}_L$ from Eq. (6.2) with the help of Eqs. (5.5) and (5.7) and the relations

$$\nabla\cdot\mathbf{v}_s=0,\quad \nabla\cdot[\hat{\mathbf{z}}\times\mathbf{v}_s]=-\hat{\mathbf{z}}\cdot[\nabla\times\mathbf{v}_s] . \tag{6.3}$$

We then obtain a nonlinear equation for the superfluid vorticity:

$$\frac{d\Omega_s}{dt}+\frac{\rho_n}{\rho}B\Omega_s(\Omega_s-\Omega)=0 . \tag{6.4}$$

In fact, this equation of motion for the superfluid vorticity is more general than can be appreciated from our derivation: As long as $\mathbf{v}_n$ is clamped to corotation at the rotation velocity Ω (expressed in the laboratory frame), Ω may here also depend explicitly on time, i.e., $\Omega=\Omega(t)$ if its time dependence is sufficiently slow to preserve the corotation of the normal component (see Appendix B 3). As depicted in Fig. 8, we concentrate on the relaxation decay after stopping the cryostat; in this case $\Omega=0$ and the solution of Eq. (6.4) gives the decay of $\Omega_s=\kappa n_v/2$:[51]

$$\Omega_s=\Omega_0/[1+(t-t_0)/\tau_F] . \tag{6.5}$$

Equation (6.5) yields the time dependence of the total vortex number in the NMR cell given by $N_v=\pi R^2 2\Omega_s/\kappa$, which corresponds to the measured signal in Fig. 8. Here $\tau_F=(B\Omega_0\rho_n/\rho)^{-1}$ is a decay time, which depends on the vortex density $n_{v0}=\Omega_0/\kappa$ at some arbitrary time $t=t_0$ after stopping rotation.

One may now determine the experimental decay time τ_F by fitting the measured signal decay to the time dependence expressed by Eq. (6.5). In Fig. 10, the result has been plotted in the form $(\tau_F\Omega_0)^{-1}$, i.e., as the dissipative mutual friction parameter $(\rho_n/\rho)B$. It appears to be consistent with earlier measurements[48] close to T_c. Presently the resolution in the measurements is not sufficient for a reliable estimate of a discontinuity in the value of B on traversing the vortex core phase transition (in Fig. 10 at

$p=29.3$ bars $T_v=0.60T_c$). Likewise, it will be interesting to study the dependence of B on pressure p and magnetic field H, which both effect gradual changes in the size and structure of the core. The influence of these variables on B is also present in the slow collective mode response, which will be discussed in Sec. VII C.

It is interesting to note that the fit of the measured fast response to Eq. (6.5) explains all of the time delay in the disappearance of the vortices in a "rapid stop experiment." This means that the final annihilation process at the side wall is short and dominated by the time required for the vortices to reach the wall. Consequently, there is no symmetry in this respect between annihilation and nucleation, since in nucleating a singular vortex core a large critical velocity is involved, which is related to the bulk liquid pair-breaking velocity.[21]

In assuming that the normal component is clamped to corotation with the container, we neglect the torque from moving vortices on the normal component. This is a good approximation if the viscosity of the normal fluid is large compared to mutual friction ($\tau_F \gg \tau_n$). The equations coupling the motion of the superfluid and normal components can be found in Ref. 51; our numerical analysis of these equations shows that in our experimental conditions Eq. (6.5) describes accurately the decay of vorticity.

VII. SLOW VORTEX MOTION

A. Kelvin wave and superfluid Ekman layer

If vortex motion is accompanied by deformations of the vortex array, then the superfluid velocity $\mathbf{v}_s$ close to the vortex line, which enters Eq. (5.5), differs from the average superfluid velocity $\mathbf{v}_s$ in Eqs. (5.6) or (5.8); the former will be called the *local* superfluid velocity and noted as $\mathbf{v}_{sl}$. One form of deformation is the bending of vortex lines, when the displacement $\mathbf{u}(z)$ of the vortex line from its equilibrium position depends on z. Bending of a vortex line increases its length and, correspondingly, its energy. As a result, a line-tension force $-E_0 d^2\mathbf{u}/dz^2$ appears which tries to restore the straight configuration of the vortex line. Here $E_0=(\rho_s\kappa^2/4\pi)\ln(r_v/r_c)$ is the energy per unit length of the vortex line. This line-tension force is similar to that of a string under tension; however, contrary to the latter, it is balanced not by the inertial force acting on the unit element of the line, but by the Magnus force proportional to the difference of the average superfluid velocity $\mathbf{v}_s$ and the local superfluid velocity $\mathbf{v}_{sl}$:

$$\kappa\rho_s[\hat{\mathbf{z}}\times(\mathbf{v}_{sl}-\mathbf{v}_s)]=-E_0\frac{d^2\mathbf{u}}{dz^2} \ . \tag{7.1}$$

The local superfluid velocity can then be written as

$$\mathbf{v}_{sl}=\mathbf{v}_s+\nu_s\left[\hat{\mathbf{z}}\times\frac{d^2\mathbf{u}}{dz^2}\right] , \tag{7.2}$$

where

$$\nu_s=\frac{E_0}{\rho_s\kappa}=\frac{\kappa}{4\pi}\ln\frac{r_v}{r_c} \tag{7.3}$$

is the line-tension parameter. Equation (5.5) for $\mathbf{v}_L$ in the clamped regime should now be rewritten in terms of the local superfluid velocity $\mathbf{v}_{sl}$:

$$\mathbf{v}_L=\left[1-B'\frac{\rho_n}{2\rho}\right]\mathbf{v}_{sl}-B\frac{\rho_n}{2\rho}[\hat{\mathbf{z}}\times\mathbf{v}_{sl}] \ . \tag{7.4}$$

A solution of Eqs. (5.8), (7.2), and (7.4) in the form of a plane wave $\propto \exp(ipz-i\omega t)$ propagating along the vortex lines gives the spectrum of the Kelvin mode:

$$\omega=\pm(2\Omega+\nu_s p^2)\left[1-\frac{\rho_n}{2\rho}B'\mp i\frac{\rho_n}{2\rho}B\right] \ . \tag{7.5}$$

The gap in the Kelvin spectrum (frequency in the long-wavelength limit $p\rightarrow 0$) arises from the collective effect due to the long-range vortex interaction, as in the case of the inertial wave in Sec. V B. The Kelvin mode is a circularly polarized wave propagating as a helical wave along an isolated vortex line.[18] The Kelvin mode influences the oscillations of a pile of disks immersed in a superfluid, which were studied intensively in the case of ^{4}He and contributed essentially to our knowledge of the hydrodynamics of rotating superfluids.[27,53] The Kelvin mode might be observed even in superfluid ^{3}He. It does not involve motion of the normal component and the large viscosity would have no effect, as damping is determined by mutual friction. Mutual friction decreases rapidly towards low temperatures and one might then expect to find well-developed Kelvin oscillations.

The Kelvin mode does not propagate as a wave if $\omega<2\Omega$, as is seen from Eq. (7.5). In the limit of very slow motion $\omega\ll\Omega$ the imaginary wave number of the Kelvin mode is given by the relation

$$p^2=-\frac{2\Omega}{\nu_s} \ . \tag{7.6}$$

This means that the low-frequency Kelvin mode does not penetrate into the bulk fluid, but is restricted within a layer with the width[13,22]

$$l_E=\sqrt{\nu_s/2\Omega} \ . \tag{7.7}$$

This layer may be called the superfluid Ekman layer in analogy with the classical Ekman layer into which the viscous motion of a rotating fluid penetrates. The width of the superfluid Ekman layer involves the quantum parameter $\nu_s=(\kappa/4\pi)\ln(r_v/r_c)$ while in the width of the classical Ekman layer it is replaced by the kinematic viscosity ν.[1,49] Correspondingly, the superfluid Ekman number $\mathcal{E}=l_E^2/L^2=\nu_s/(2\Omega L^2)$ may be introduced. The term "superfluid Ekman number" was suggested by Alpar[54] while analyzing empirical expressions for the relaxation time of superfluid ^{4}He after a sudden spontaneous spin up of the container. This question arose in the context of the measurements by Tsakadze and Tsakadze,[55] who attempted to establish a connection between vortex motion and pulsar glitches with their measurements. However, Alpar used the circulation quantum κ instead of the line-tension parameter ν_s.

The Ekman layer is a result of long-range interaction between vortices, like the Debye layer in a plasma is due to the long-range Coulomb interaction: Deviations from quasineutrality in a plasma are restricted to the Debye layer. Similarly, deviations from columnar slow motion of vortices are possible only within the Ekman layers at the top and bottom walls of the container.[13]

The superfluid Ekman layer is important also for vortices in the mixed state of type-II superconductors. When the external magnetic field is not normal to the surface of a superconductor, the vortex lines should be parallel to the magnetic field in the bulk superconductor, but normal to the surface. As a result of these two competing tendencies, the vortex lines are bent within some surface layer. When the magnetic penetration length is much larger than the intervortex distance, i.e., the magnetic field is well above the lower critical field, the width of this layer in terms of the intervortex distance and the core radius is identical to that of the superfluid Ekman layer (see Ref. 56). Thus, the superfluid Ekman layer is a general concept, which is relevant for a vortex array in any superfluid or superconductor. Here it is explicitly introduced for the discussion of collective pinning in Sec. VII D.

B. Surface pinning

Vortex motion in the superfluid is resisted by pinning at the top and bottom walls of the rotating container. The pinning force originates from the roughness of the solid surface. Suppose that the surface profile is given by the height distribution $h(\mathbf{r})$, measured from some average level along the $\hat{\mathbf{z}}$ direction (h is negative for a bulge on the surface). Here $\mathbf{r}$ is a position vector in the xy plane. Consider a single vortex line in a large container (Fig. 11): How does its energy vary with its position on the pinning surface? If pinning is weak, a moving vortex remains approximately straight and its energy varies proportional to the energy E_0 per unit length:

$$\Delta E = E_0 h(\mathbf{r}) \ . \tag{7.8}$$

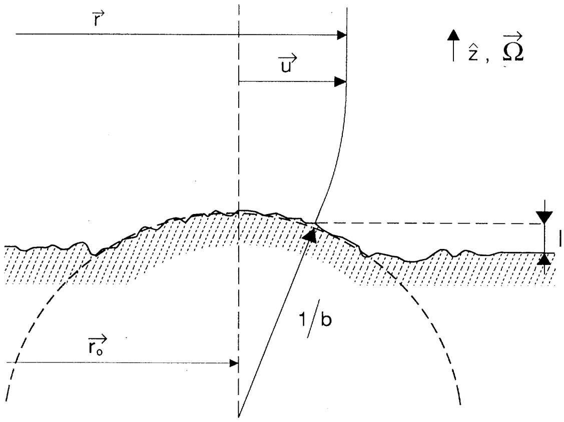

FIG. 11. Pinning of an isolated vortex line on the bottom surface of the rotating container. In the linear pinning regime surface roughness is characterized by a protuberance with a radius of curvature $1/b$: the pinning force $\mathbf{f}_p = -b\mathbf{u}$ depends on the displacement $\mathbf{u}$ from the summit of the protuberance. This gives a harmonic pinning well for the pinning energy as a function of displacement. In the weak pinning limit the pinning strength b is small, the radius $1/b$ is large, and the resulting curvature of the vortex line is small. In writing Eq. (7.9), the small curvature of the vortex line is neglected.

The elastic force on the vortex (the elastic-pinning force) is

$$\mathbf{f}_p = -E_0 \frac{dh(\mathbf{r})}{d\mathbf{r}} \ . \tag{7.9}$$

The pinning force attracts the end point of the vortex to summits of surface protuberances. However, this is resisted by forces on the vortex line in the bulk. The momentum transferred by the bulk forces to the vortex is then transported to the surface by the elastic momentum flux $-E_0 d\mathbf{u}/dz$ proportional to the line-tension E_0. Here $\mathbf{u}$ is the displacement of the vortex line, measured in the xy plane. The balance of forces at the top and bottom surfaces is

$$\mathbf{f}_p^{\pm} = \pm E_0 \frac{d\mathbf{u}}{dz} \quad \text{at } z = \pm L/2 \ . \tag{7.10}$$

The signs $\pm$ correspond to the top ($z = +L/2$, the upper sign) and the bottom ($z = -L/2$, the lower sign) of the container, respectively. With the help of Eq. (7.9), this gives the boundary conditions

$$-\frac{dh(\mathbf{r})}{d\mathbf{r}} = \pm \frac{d\mathbf{u}}{dz} \ . \tag{7.11}$$

Suppose that the end of the vortex line is not very far from the summit of the protuberance [the minimum of $h(\mathbf{r})$ at $\mathbf{r} = \mathbf{r}_0$ in Fig. 11], so that one can expand $h(\mathbf{r}) = h(\mathbf{r}_0 + \mathbf{u})$. For simplicity we assume that the protuberance is axisymmetric. Then

$$h(\mathbf{r}) \simeq h(\mathbf{r}_0) + \frac{1}{2}\frac{d^2h}{dr^2}u^2 \ , \tag{7.12}$$

and the linearized version of the boundary condition Eq. (7.11) is

$$\frac{d\mathbf{u}}{dz} = \mp b\mathbf{u} \tag{7.13}$$

with $b = d^2h/dr^2$ being equal to the inverse of the radius of curvature of an axisymmetric protuberance,[50] as sketched in Fig. 11. Equation (7.13) gives the elastic-pinning condition. It is reminiscent of the boundary condition, which was suggested by Hall[27] for the slippage of vortices relative to the solid surface in terms of a viscous surface force. In a more general form proposed by Bekarevich and Khalatnikov[57,58] the slip boundary condition is

$$\frac{d\mathbf{u}}{dz} = \mp (b_1 \mathbf{v}_L + b_1' [\hat{\mathbf{z}} \times \mathbf{v}_L]) \ . \tag{7.14}$$

In the case of the slow mode governed by weak pinning the transverse viscous surface force $\propto [\hat{\mathbf{z}} \times \mathbf{v}_L]$ is of no importance, since vortex motion is linearly polarized throughout the whole fluid (both the displacement $\mathbf{u}$ and the velocity $\mathbf{v}_L = \partial\mathbf{u}/\partial t$ are azimuthally oriented). In this case we can generalize the boundary condition to incorporate both elastic and viscous surface forces, but no transverse components:

$$\frac{d\mathbf{u}}{dz}=\mp(b\mathbf{u}+b_1\mathbf{v}_L)\ . \tag{7.15}$$

While applying the boundary condition Eq. (7.15) to the analysis of the slow vortex mode in the next section, we shall find that the two parameters b and b_1 affect the vortex dynamics differently: while b is crucial for the existence of the slow vortex mode, governed by pinning, b_1 only contributes to the overall losses from bulk mutual friction. Thus, the presence of the elastic-pinning contribution leads directly to the existence of the slow mode. The only measurement on the pinning parameters b and b_1, which we know of, is an experiment by Tsakadze[59] on the slow vortex mode response. He recorded the damped oscillatory rotation decay of a freely rotating light container filled with ^{4}He-II and extracted the result $b \sim 20-40\ \mathrm{cm}^{-1}$, depending on the surface preparation. Our result for ^{3}He-B on an epoxy surface is $b \sim 1\ \mathrm{cm}^{-1}$ (Sec. VII D).

C. Slow vortex mode

In slow vortex motion bending is confined to the Ekman layers adjacent to the top and the bottom walls of the container; a study of the slow mode thus has to address separately the regions outside and inside the Ekman layers. In the bulk vortices perform columnar motion and remain straight with good accuracy; within the Eckman layers Kelvin modes, which involve vortex bending, are excited due to surface pinning. This analysis has been done for ^{4}He (Ref. 22) (see also Ref. 13). It yielded a slow mode with a frequency much lower than the angular velocity of rotation: $\omega \ll \Omega$. Here we present the analysis for ^{3}He, which differs from that for ^{4}He in two aspects.[50]

(1) In ^{3}He, vortices perform slow motion in the clamped regime: $\mathbf{v}_n=0$ in the frame of the rotating cryostat.

(2) In ^{3}He surface pinning is expected to be weaker.

The latter feature of slow motion in ^{3}He permits us to simplify the analysis of the slow motion essentially. Averaging Eq. (7.2) over the z axis, we have

$$\mathbf{v}_{sl}=\mathbf{v}_s+\frac{\nu_s}{L}\left[\hat{\mathbf{z}}\times\left[\left.\frac{d\mathbf{u}}{dz}\right|_{z=L/2}-\left.\frac{d\mathbf{u}}{dz}\right|_{z=-L/2}\right]\right]\ . \tag{7.16}$$

The inclination $d\mathbf{u}/dz$ of the vortex line near the top and the bottom of the container is determined from the phenomenological boundary condition Eq. (7.15) imposed on the vortex displacement. If pinning is weak, vortex bending is weak not only in the bulk fluid but also in the Ekman layers [we shall derive the condition of weak pinning later, see Eq. (7.35)], i.e., moving vortices remain nearly straight throughout the whole container. For now we may simply assume that the vortex displacement at the transverse wall, given by Eq. (7.15), does not differ seriously from the displacement anywhere in the bulk fluid, i.e., the displacement $\mathbf{u}(z,t)$ only weakly depends on z and the position of the vortex line is defined by one two-dimensional position vector $\mathbf{u}(t)$. Then the difference between the local and average superfluid velocities is

$$\mathbf{v}_{sl}-\mathbf{v}_s=-\frac{2\nu_s b}{L}[\hat{\mathbf{z}}\times\mathbf{u}]-\frac{2\nu_s b_1}{L}[\hat{\mathbf{z}}\times\mathbf{v}_L]\ . \tag{7.17}$$

Thus, all the z variations of the fluid parameters are excluded and the problem becomes two dimensional. The next step is to find a solution in the form of a plane wave $\sim\exp(i\mathbf{q}\cdot\mathbf{r}-i\omega t)$, similar to the derivation given in Ref. 13. However, we consider the limit $q\rightarrow 0$ here. In fact, the wave vector $\mathbf{q}$ is only necessary for pointing the direction in which an incompressible fluid cannot move: the component of $\mathbf{v}_s$ along $\mathbf{q}$ should vanish since $\nabla\cdot\mathbf{v}_s=0$. In a cylinder it is the radial component of $\mathbf{v}_s$. On excluding the average and the local superfluid velocities $\mathbf{v}_s$ and $\mathbf{v}_{sl}$ from Eqs. (5.8), (7.4), and (7.17), one obtains a system of two equations for the components of the vortex velocity along the wave vector $\mathbf{q}$ (the component v_{Lq}) and normal to it (the component v_{Lt}):

$$v_{Lq}\left[i\omega-\frac{\rho_n}{\rho}B\Omega\right]+v_{Lt}\omega_\Sigma\left[1-\frac{\rho_n}{2\rho}B'\right]=0\ , \tag{7.18}$$

$$-v_{Lq}2\Omega\left[1-\frac{\rho_n}{2\rho}B'\right]+v_{Lt}\left[i\omega-\frac{\rho_n}{2\rho}B\omega_\Sigma\right]=0\ . \tag{7.19}$$

The frequency

$$\omega_\Sigma=\frac{2\nu_s}{L}(b-i\omega b_1) \tag{7.20}$$

incorporates both the elastic and viscous surface forces. This frequency is much smaller than the angular velocity Ω. In the case of axisymmetric vortex motion in a cylindrical container, the q component and the t component correspond to the radial and azimuthal components of the vortex velocity, respectively. The set of Eqs. (7.18) and (7.19) can now be used to characterize both the fast mutual-friction-resisted motion and the slow mode. The dispersion equation for this system of two equations is

$$\omega^2+i\omega\frac{\rho_n}{2\rho}B2\Omega-2\Omega\omega_\Sigma\left[\left[1-\frac{\rho_n}{2\rho}B'\right]^2+\left[\frac{\rho_n}{2\rho}B\right]^2\right]=0\ . \tag{7.21}$$

Let us first briefly consider the fast mutual-friction-resisted mode in its linear regime at finite $\Omega_s=\Omega$. This mode corresponds to the larger value $\omega\sim\Omega$ of the two roots of the dispersion equation (7.21). Neglecting the elastic frequency ω_Σ, this root is

$$i\omega=\frac{1}{\tau_F}=\frac{\rho_n}{\rho}B\Omega \tag{7.22}$$

and represents exponential relaxation, $\propto\exp(-t/\tau_F)$, which describes the approach of the vortex density to its new equilibrium value in the spin-up or spin-down experiments. Indeed, one can see from Eq. (7.19) that

$$\frac{v_{Lq}}{v_{Lt}}=\frac{i\omega}{2\Omega[1-(\rho_n/2\rho)B']}=\frac{(\rho_n/2\rho)B}{1-(\rho_n/2\rho)B'}\ , \tag{7.23}$$

i.e., the ratio of the normal to the transverse components of the vortex velocity depends on the relative magnitude of the mutual friction parameters only. Since the dissipation parameter B is not equal to zero anyway, the fast frictional mode always involves the radial motion in a cylindrical container (the velocity component v_{Lq}), i.e., an expansion or contraction of the vortex array ultimately leads to a rearrangement of the vortex density towards a new equilibrium value. At the same time, the vortices move spirally in general, since the azimuthal component v_{Lt} is also present, excluding the special case $1-(\rho_n/2\rho)B'=0$.

The smaller root of the dispersion equation (7.21) gives the slow mode. In order to find the low-frequency branch of the spectrum we may neglect the term ω^2. Then

$$\omega=-\frac{i\omega_\Sigma}{\beta} . \tag{7.24}$$

Here a new pair of mutual friction parameters is introduced:

$$\beta=\frac{(\rho_n/2\rho)B}{[1-(\rho_n/2\rho)B']^2+[(\rho_n/2\rho)B]^2} ,$$
$$\beta'=\frac{1-(\rho_n/2\rho)B'}{[1-(\rho_n/2\rho)B']^2+[(\rho_n/2\rho)B]^2} . \tag{7.25}$$

Since ω_Σ depends on the frequency ω of the slow mode in Eq. (7.20), Eq. (7.24) is a linear equation for ω. Its solution yields

$$i\omega=\frac{2\nu_s b}{\beta L+2\nu_s b_1} . \tag{7.26}$$

This equation shows that the elastic pinning force $-bE_0\mathbf{u}$ is responsible for the slow vortex mode, even though it is weak. However, the weak pinning force is of minor importance in the case of the last frictional mode: the frequency characterizing the pinning force ω_Σ is large in comparison to $1/\tau_s$ but small when compared to $1/\tau_F$. The elastic pinning force exists only in the pinned state of the vortex array, when any vortex moves in vicinity of some pinning site. At large drives vortices are depinned and have no tight connection with any individual pinning site. Then their interaction with a rough surface produces only a viscous force as in the Bekarevich-Khalatnikov boundary condition Eq. (7.14) and the slow mode does not exist. In the measurements we frequently make use of a harmonically modulated rotation drive. It is helpful to think about pinning in this context as exemplified in Fig. 12. Here the strength of the pinning force is shown as a function of the amplitude $\Delta\Omega$ of the harmonic component in Ω at a drive frequency ω_m which couples to both modes, $1/\tau_s<\omega_m<1/\tau_F$. At small $\Delta\Omega$ the vortex displacements are small and the pinning force is proportional to the displacement (linear regime). With increasing $\Delta\Omega$ this linearity is lost, the effective pinning parameter decreases and the pinning force increases more slowly with displacement, as the end of the vortex line approaches the edge of the potential well associated with a given pinning site. Eventually at still larger $\Delta\Omega$ the vortex slides over the edge of the well and becomes depinned. In the depinned state the vortex slides relatively freely over the top and bottom surfaces of the container, in a manner which might be called "plastic flow." In the plastic flow regime the elastic-pinning force vanishes and the slow mode does not exist. The threshold between the pinned and depinned states may be viewed as a phase transition in a random system. As opposed to the slow mode, the fast mode is not sensitive to pinning and exists at any drive amplitude $\Delta\Omega$. However, at small $\Delta\Omega$ and low drive frequency ω_m it is shadowed by the slow mode. The dependence of the amplitude of the measured resonance signal on $\Delta\Omega$ is discussed in Appendix B.

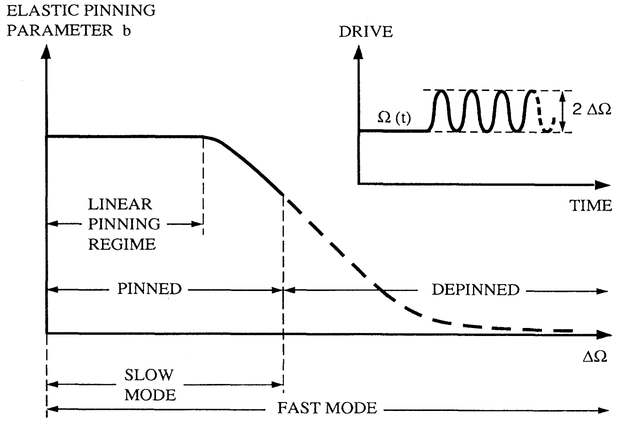

FIG. 12. Vortex motion and pinning in the presence of a sinusoidally varying rotation drive. At very small $\Delta\Omega$ the slow mode is excited in the linear pinning regime where the restoring force is the harmonic pinning force $f_p=-bu$. It depends linearly on the displacement u of a given vortex from the center of its pinning well. When the drive amplitude $\Delta\Omega$ is increased pinning becomes weaker and in the other extreme the vortices are in a depinned state. Here the ends of the vortex lines slide over the top and bottom surfaces of the rotating container in a manner which resembles the plastic flow of dislocations in a crystalline solid under stress.

The viscous pinning force $-b_1E_0\mathbf{v}_L$ is not of crucial importance for the existence of the slow vortex mode: it simply adds to the bulk mutual friction losses $\propto\beta L$, since the total losses are proportional to $\beta L+2\nu_s b_1$. We may estimate the relative importance of the surface losses $\nu_s b_1/(\beta L)$ using a value for the slip parameter $1/b_1$ measured by Tsakadze[59] for superfluid ^{4}He: His most reliable pair of pinning parameters appears to be $b\sim40$ cm^{-1} and $b_1\sim10$ s/cm^{-2}. This yields a rough estimate $\nu_s b_1/(\beta L)\sim\frac{1}{2}$ at about $T\sim T_c/2$ in ^{4}He-II. In ^{3}He pinning forces, both elastic and viscous, are expected to be weaker while mutual friction is higher. In fact, using $b_1\sim10$ s/cm^{-2}, we obtain $\nu_s b_1/(\beta L)\sim\frac{1}{40}$ for the comparable ratio in ^{3}He-B. Thus, it appears that we may neglect b_1. The exponential relaxation time of the slow mode is then given by

$$\frac{1}{\tau_c}=i\omega=\frac{2\nu_s b}{\beta L} . \tag{7.27}$$

Referring to Eq. (7.18) we may again determine the ratio of the radial and azimuthal components of the vortex velocity:

$$\frac{v_{Lq}}{v_{Lt}}=\frac{\omega_\Sigma}{2\Omega}\frac{1-(\rho_n/2\rho)B'}{(\rho_n/2\rho)B}=\frac{i\omega\beta'}{2\Omega} . \tag{7.28}$$

Thus, the radial velocity is smaller by the factor $\omega_\Sigma/\Omega \ll 1$ than the azimuthal velocity. In contrast to the elliptically polarized fast frictional mode and the circularly polarized Kelvin mode, the polarization of the slow mode is close to linear: in a cylinder it involves predominantly azimuthal motion at nearly constant vortex density.

During the slow mode the stable pattern is restored in the vortex array, determined both by pinning and by the interactions between vortices. The character of this collective process is essentially different than the case when a single vortex is approaching a single pinning site. The latter process may be described by the equations of this section assuming that the liquid as a whole is at rest, i.e., $\mathbf{v}_s=0$, $\Omega=0$. After inserting Eq. (7.17) into Eq. (7.4) one obtains, instead of Eqs. (7.18) and (7.19),

$$v_{Lx}\left[i\omega-\frac{\rho_n}{2\rho}B\omega_\Sigma\right]+v_{Ly}\omega_\Sigma\left[1-\frac{\rho_n}{2\rho}B'\right]=0 , \tag{7.29}$$

$$-v_{Lx}\omega_\Sigma\left[1-\frac{\rho_n}{2\rho}B'\right]+v_{Ly}\left[i\omega-\frac{\rho_n}{2\rho}B\omega_\Sigma\right]=0 . \tag{7.30}$$

Since now there is no superfluid velocity $\mathbf{v}_s$ induced by other vortices, there is no preferable direction $\mathbf{q}$. In order to emphasize this we use components x and y instead of q and t. The eigenfrequency of the single-vortex mode is

$$\omega=\pm\omega_\Sigma\left[1-\frac{\rho_n}{2\rho}B'\mp i\frac{\rho_n}{2\rho}B\right] , \tag{7.31}$$

and the relation between the velocity components is

$$v_{Ly}=\mp i v_{Lx} . \tag{7.32}$$

Equation (7.31) is the frequency of the Kelvin mode, Eq. (7.5), with the collective effect neglect ($\Omega=0$) and the wave number p determined by the boundary condition from pinning. Thus, the time dependence and trajectory of motion are different for the slow collective mode and for the single-vortex mode. Whereas the motion of a vortex in the slow collective mode is azimuthal, in the single-vortex mode a vortex approaches the pinning site along a spiral trajectory: the vortex rotates around the pinning site with the angular velocity

$$\omega_R=\omega_\Sigma\left[1-\frac{\rho_n}{2\rho}B'\right]=\frac{2\nu_s b}{L}\left[1-\frac{\rho_n}{2\rho}B'\right] \tag{7.33}$$

and its distance from the pinning site is exponentially decreasing as $\exp(-t/\tau_s^*)$ with the relaxation time given by [cf. Eq. (7.27)]

$$\frac{1}{\tau_s^*}=\frac{\rho_n}{2\rho}B\omega_\Sigma=\frac{\rho_n}{2\rho}B\frac{2\nu_s b}{L} . \tag{7.34}$$

Let us next derive the condition for the validity of the weak pinning assumption, which is the basis for our analysis of the slow motion. The vortices are assumed to be straight, but owing to their binding in the Eckman layers there is a difference between vortex displacement in the bulk and that on the surface; the difference is of order $l_E du/dz=bl_E u$. Pinning is weak when this difference is smaller than the displacement u itself. This gives the condition of weak pinning:

$$b \ll \frac{1}{l_E} . \tag{7.35}$$

The conditions restricting the validity of weak pinning are very different for the slow mode of a vortex array ($\omega \ll \Omega$) and the Kelvin mode of a single-vortex line ($\omega \gg \Omega$, when collective effects are not important). For the single-vortex Kelvin mode given by Eqs. (7.31) and (7.32) bending is not confined to the superfluid Ekman layer: the difference between vortex displacement in the bulk and that on the surface is of order $L du/dz \approx Lbu$. Then the condition of weak pinning is $b \ll 1/L$, which is much stronger than Eq. (7.35), if $L \gg l_E$. The Ekman layer is not directly represented in the frequency of the slow vortex mode in the weak pinning limit, but it is explicitly present in the condition which defines weak pinning.

In associating the measured exponential relaxation time τ_s with Eq. (7.27) we note that the amplitude of the HPD absorption signal is insensitive to the sign of the driving perturbation, i.e., whether the drive corresponds to acceleration or deceleration of Ω, as can be seen from Fig. 9. Invoking linear hydrodynamics with linear responses, we relate the observed time constant with quadratic response, i.e., the measured τ_s corresponds to $\tau_c/2$, with τ_c given by Eq. (7.27). Next suppose B' is small enough to be neglected,[42] then we find that the measured temperature dependence of $(\rho_n/\rho)B$ (dashed curve in Fig. 10) adequately accounts for that of τ_s (solid curve in Fig. 13).

The measured τ_s proves to be only weakly dependent on the liquid pressure, as shown in Fig. 14. Obviously here the reproducibility and precision of our measurement is not sufficient to discern a pressure dependence. In contrast, the dependence on the external magnetic field appears to be larger, as shown in Fig. 15. This dependence may, perhaps, be explained in the framework of the discussion presented in Ref. 42. It has been shown there that the most important mechanism contributing to the mutual friction parameter B is the scattering of the quasiparticles in the bulk liquid by the quasiparticles localized in bound states in the hard vortex core. It is difficult to imagine that comparatively low magnetic fields in the experiment are able to affect the bound states in the hard core, but probably bound states in the soft vortex core also contribute to mutual friction (these states were not analyzed in Ref. 42). On increasing the magnetic field the radius of the soft core decreases. This might explain the increase of τ_s with H in Fig. 15. One might think that the soft core also contributes to the surface pinning constant b. However, on increasing the

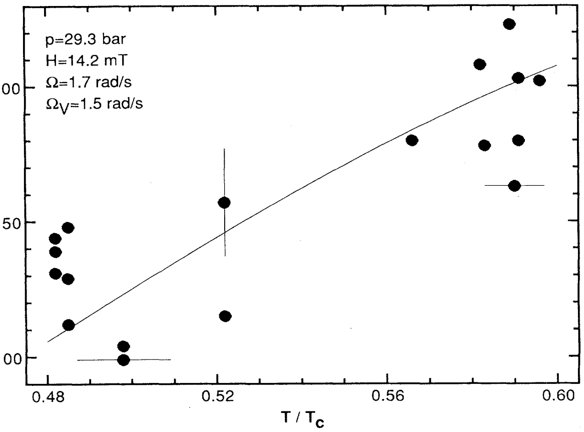

FIG. 13. Temperature dependence of the measured time constant τ_s of the slow vortex mode. The solid curve shows the expected temperature dependence according to Eq. (7.27), using for $(\rho_n/\rho)B$ the dashed line in Fig. 10 and $B'=0$. The line is thus a one-parameter fit for the pinning strength, yielding $b=0.84\ \mathrm{cm}^{-1}$.

magnetic field the soft core radius decreases, b increases and τ_c is expected to decrease, which disagrees with the observed dependence.

D. Collective pinning

An important outcome from the present work is clear evidence for collective effects in pinning. If isolated noninteracting vortices are pinned at the solid wall of the cell, the pinning parameter b does not depend on vortex density n_v or angular velocity Ω. Then, according to Eq. (7.27), the relaxation time $\tau_s=\tau_c/2$ of the slow mode depends only weakly on Ω via $v_s \propto \ln\Omega$ [see Eq. (7.3) where $r_v \propto 1/\sqrt{\Omega}$]. However, experimentally it is found that τ_s does depend on Ω and this dependence is opposite to that from the weak logarithmic dependence of v_s. The resolution in the time constant measurement and the existence of the dependence on Ω is demonstrated in Fig. 16, showing two pairs of consecutive measurements, obtained in the same measuring session immediately one after another with a minimum of changes in the experimental settings.

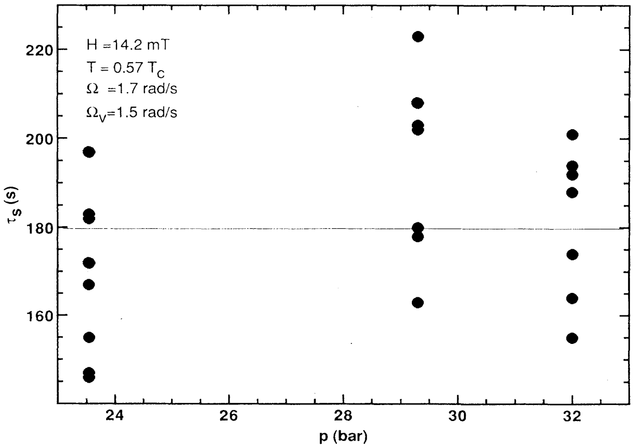

FIG. 14. Pressure dependence of the measured time constant τ_s. The solid line is an average through the data points and illustrates that no dependence can be distinguished within the experimental resolution.

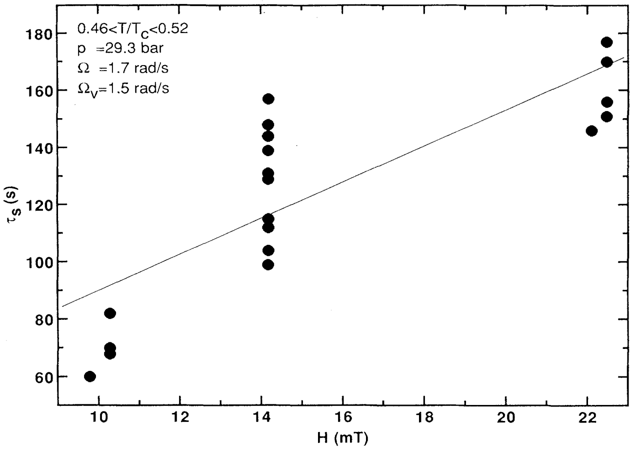

FIG. 15. Magnetic field dependence of the measured time constant τ_s. The solid line is a linear fit through the data points and illustrates a strong dependence at these low magnetic fields, which are only up to an order of magnitude larger than the dipolar field.

In this case the resolution in the measurement of the time constant τ_s is better than ±10 s. Figure 17 shows a compilation of the measurements on the time constant τ_s as a function of the vortex density $n_v=2\Omega/\kappa$. Here with data from many different runs the overall precision in the time constant measurement is poorer, perhaps ±30 s, but the central conclusion nevertheless survives: The time constant τ_s increases with increasing density, indicating that the vortices become less rigidly fixed to their pinning sites and that the pinning parameter b in Eq. (7.27) decreases with increasing density. We regard this experimental conclusion as very reliable, in spite of the fact that the measuring uncertainties may cast some doubt on the quantitative amount of the increase in τ_s with n_v.

The decrease in pinning with increasing density we ascribe to collective effects. Only at very low vortex density can one talk about isolated vortex lines, which are pinned independently. When the density increases, pinning becomes collective: correlated groups of vortices move coherently over a random distribution of abundant pinning sites. The correlated motion is brought about by the binding from the increased rigidity of the vortex array with respect to shear deformations in the transverse xy plane. The increased rigidity at higher density means that coherence, extending over a correlation length l_c, becomes increasingly important and causes a reduction in the pinning strength. This implication from Figs. 16 and 17 allows us now to speak of a vortex lattice with crystalline order extending over a length scale of order l_c.

Collective pinning was invented for the bulk pinning of quantized flux lines in superconductors, where their pinning at the defects of the crystalline lattice is similarly reduced with increasing density of the flux line lattice.[26] Collective effects in the pinning of vortices in superfluid ^{4}He have not been explicitly discussed, but their presence is suggested by at least the measurements of the thermorotational effect by Yarmchuk and Glaberson.[60] Here we thus report the first quantitative experimental evidence for long-range order and collective surface pinning in a vortex lattice.

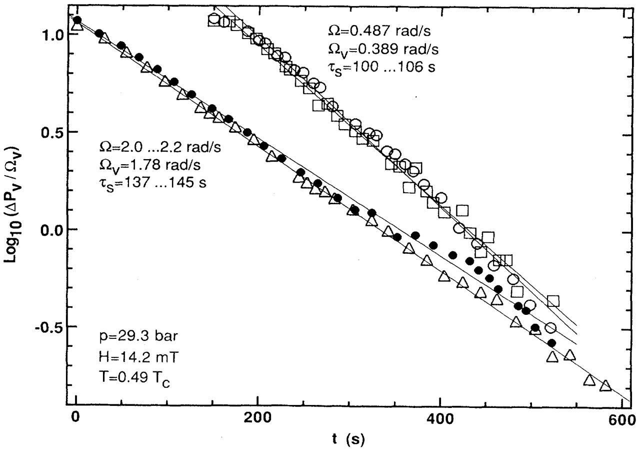

FIG. 16. Demonstration of the increase in τ_s with increasing vortex density. Four sets of measurements of the exponential relaxation time τ_s have been plotted in terms of the normalized absorption increment $\log_{10}(\Delta P_v/\Omega_v)$ as a function of time. All four measurements have been performed in as similar conditions as possible, immediately following each other, in order to reduce scatter introduced from changes in external conditions. The high-density data have been measured with the number of vortices corresponding to $\Omega_v=1.78$ rad/s: △, $\Omega=2.22$ rad/s and $\tau_s=137$ s; ●, $\Omega=2.02$ rad/s and $\tau_s=145$ s. They should be compared to the low-density measurements, for which the number of vortices corresponds to $\Omega_v=0.389$ rad/s and their density to $\Omega=0.487$ rad/s: □, $\tau_s=106$ s; ○, $\tau_s=100$ s (for these latter data the $t=0$ point has been shifted by 150 s to the right). The measurements have been performed as shown in Fig. 9; the zero point on the horizontal axis corresponds to the moment when the sinusoidal modulation of the drive is switched off (amplitude of modulation $\Delta\Omega=0.20$ rad/s and period 30 s). On the vertical scale ΔP_v is given in pW. The relative precision in the measurement of τ_s in these four examples is estimated to be better than ±10 s. The conclusion from this comparison is that τ_s increases by 40% when the vortex density increases by a factor of 4.

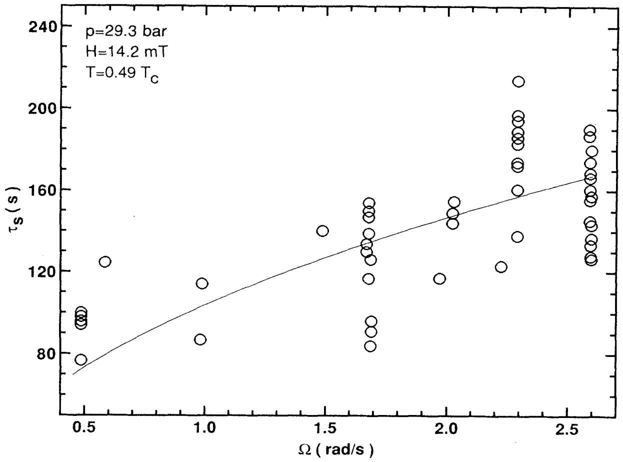

FIG. 17. Measurement of the dependence of the time constant τ_s on vortex density. Here τ_s is measured as a function of Ω for vortex clusters of varying size, but well isolated from the cylindrical container wall. The solid curve represents the fit $\tau_s=110\sqrt{\Omega}$ s. The increasing trend of τ_s we connect with a decreasing pinning strength with increasing vortex density, as expected in collective pinning. The overall accuracy in the determination of τ_s is ±30 s in this plot with measurements from many different experiments.

Let us now work through some qualitative scaling arguments which provide a simple semiquantitative explanation for the results in Figs. 16 and 17 in terms of collective pinning. At very low Ω the pinning strength $b=b_s$ is the static pinning parameter of a single isolated vortex line. With increasing Ω the emergence of the vortex lattice is manifested by the increasing correlation in the motion of the vortices, characterized by a correlation length l_c. The number of vortices within a correlated group is given by the areal ratio $N_c \approx (l_c/r_v)^2$ where $r_v \approx n_v^{-1/2}$ is the intervortex distance. Assuming that the density of pinning sites exceeds the vortex density, then each vortex interacts mainly with its own nearest pinning site. Thus, N_c coherently moving vortices interact with approximately N_c pinning forces. Because of the random directions of these pinning forces, the resultant random force on the N_c correlated vortices is of order $\sqrt{N_c}$ and not N_c times larger than the typical pinning force acting on a single vortex. This is illustrated in Fig. 18 and means that in collective pinning the pinning per one vortex is reduced by the factor $1/\sqrt{N_c}$. The pinning parameter b is now estimated as

$$b \approx \frac{b_s}{\sqrt{N_c}} = \frac{r_v}{l_c} b_s \ . \tag{7.36}$$

The correlation length l_c is defined by the balance between the energy gain from selecting the best position for the correlated group of vortices in their random pinning sites and the loss incurred from the inevitable deformations of the vortex lattice. The pinning energy per one vortex is proportional to the increase in vortex length and is of order

$$E_p \sim b E_0 u_0^2 \sim \frac{r_v}{l_c} b_s E_0 u_0^2 \ . \tag{7.37}$$

Here u_0 is the static vortex displacement, in contrast to the dynamic displacement $u(t)$ discussed earlier (see Fig. 18). The elastic energy density of the vortex lattice per unit volume with respect to shear deformations in the xy plane, i.e.,

$$\epsilon = \frac{1}{2}\left[\frac{\partial u_{0x}}{\partial y} + \frac{\partial u_{0y}}{\partial x}\right] , \tag{7.38}$$

is given by[13]

$$\mathcal{E}_{\rm el} = \rho_s \kappa \Omega \epsilon^2 \ .$$

Only shear deformations of the form defined by Eq. (7.38) participate in collective pinning, since compression of the vortex lattice is energetically very expensive.[26] In the correlated vortex group the single-vortex displacement u_0 is smeared out over the coherent region and thus the scale over which the displacement varies becomes $\sim l_c$ and $\epsilon \approx u_0/l_c$. Shear deformation of the vortex lattice near the top and bottom surfaces is inevitably accompanied by vortex bending which heals the distortions of the vortex lattice. The healing length is the Ekman layer width $l_E = \sqrt{\nu_s/2\Omega}$ [Eq. (7.7)] as shown in Fig. 18. Thus, elastic deformation is confined within the Ekman layer and the elastic deformation energy per vortex line can be written as

$$E_{\rm el} \approx \mathcal{E}_{\rm el} l_E r_v^2 \approx \rho_s \kappa^2 \frac{u_0^2}{l_c^2} l_E \approx \frac{l_E E_0}{l_c^2 \ln(r_v/r_c)} u_0^2 \ . \qquad (7.40)$$

The correlation length l_c is determined by minimizing the sum of the pinning energy $-E_p$ (negative) and the elastic energy $E_{\rm el}$ (positive). Their sum is minimized, when $E_p \sim E_{\rm el}$, and one then obtains the coherence length

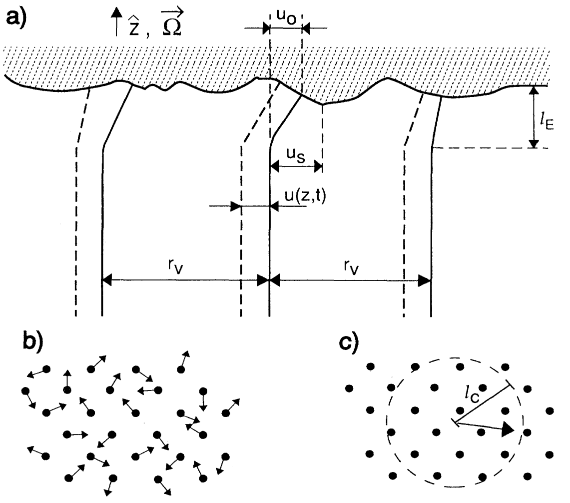

FIG. 18. Collective pinnning of vortex lines in the slow vortex mode. (a) Viewed from the side, three vortex lines are pinned to the top surface of the cell, shown with dashed lines in their displaced positions during the slow motion and with solid lines in their final stationary positions. In the weak pinning limit the bending of vortex lines is much less than illustrated here. (b) Viewed from above, the pinning forces act randomly in a correlated group of N_c vortices. (c) The randomly oriented pinning forces can be united to give a resultant random pinning force, which acts on a group of vortices glued together by the shear elasticity of the vortex lattice over the correlation length l_c. Here $u(z,t)$ is the dynamic displacement of the vortex from its equilibrium position while u_0 measures the displacement of the end of the vortex line from its position in the bulk regular lattice. The displacement u_0 is determined by the pinning relief averaged over the scale l_c and does not correspond in general to the position of minimum pinning energy at any pinning site. The displacement u_s is measured from the minimum pinning energy position for a single vortex line (like u in Fig. 11 in Sec. VII B).

$$l_c = \frac{l_E}{r_v b_s} \frac{1}{\ln(r_v/r_c)} \ , \qquad (7.41)$$

which is independent of Ω if the slowly varying logarithmic term is neglected. Keeping in mind that according to Eq. (7.36), $b \propto 1/\sqrt{\Omega}$ (since $r_v \propto 1/\sqrt{\Omega}$) and that according to Eq. (7.27), $\tau_s = \tau_c/2 \propto 1/b$, we thus see that $\tau_c \propto \sqrt{\Omega}$, which justifies the curve fitted through the data points in Fig. 17. Collective pinning is a valid concept when the number of correlated vortices is sufficiently large, i.e., when $l_c \gg r_v$. It is not difficult to show that this condition, in fact, coincides with the condition for weak pinning in Eq. (7.35). Thus, weak surface pinning is always collective.

Summarizing our qualitative analysis we note that with increasing Ω a crossover from the pinning of isolated vortex lines with $b = b_s \geq 1/l_E$ takes place at rather low Ω and one then passes in the range of collective pinning with $b \approx r_v^2 b_s^2 \ln(r_v/r_c)/l_E \ll 1/l_E$. If we compare the fitted square-root dependence $\tau_s \approx 110\sqrt{\Omega}$ s in Fig. 17 with Eq. (7.27) we obtain for the pinning parameter $b \approx 0.8$ cm^{-1} at $\Omega = 2$ rad/s. This satisfies the weak pinning condition $b \ll 1/l_E \approx 100$ cm^{-1}, in other words the radius of curvature associated with pinning is 2 orders of magnitude larger than the width of the Ekman layer and the bending of the vortex lines is restricted to a very low level indeed. The estimate for the correlation length l_c is of order ten lattice spacings, on the basis of these simple scaling arguments.

The slow mode, being governed by pinning, is related to surface roughness on some appropriate scale, irrespective of collective effects. To define this scale we need the single-vortex pinning parameter b_s in Eq. (7.36). With $b_s \sim b l_c/r_v \approx 10$ cm^{-1}, the scale of roughness is $\sim 1/b_s \approx 1$ mm. This estimate shows that the scale $1/b_s$ is very large compared to the core size and, in fact, exceeds the typical intervortex distance. The latter may be explained as an artifact from the approximations in the scaling arguments. The displacements of the vortices during the observation of the slow mode are well within the length scale $1/b_s$, i.e., a vortex moves within one and the same pinning site. This is an important property: it allows the observation of the slow mode over a time span of several time constants τ_s.

It is interesting to note that weak pinning is also indicated by the fact that remnant vortices have not been observed in our NMR cell after rotation has been stopped and the vortices have been allowed to annihilate over a waiting period of a few minutes in stand still.[21] This means that the amount of remnant vorticity at that point is below our sensitivity threshold, i.e., the equivalent of 20 rectilinear vortices or less. In superfluid ^{4}He, where pinning is stronger, remnant vorticity has been reported in various situations after a history of rotation[20] and even in the absence of rotation, simply after cooling through the λ transition.[35]

The fact that pinning is stronger in ^{4}He than in ^{3}He-*B* is also indicated by a comparison of their respective slow vortex mode responses. In ^{4}He a measurement of the slow vortex mode has been carried out by Tsakadze[59] in experimental conditions comparable to our case where no contribution from bulk shear elasticity is expected (Appendix D). In a container with an aspect ratio $L/(2R) \leq 2.3$ he found a damped oscillatory response, governed by surface pinning. At $\Omega = 6$ rad/s he extracted a pinning strength of $b \sim 30$ cm^{-1}. This result means that with an Ekman layer width of $l_E \sim 10^{-2}$ cm the ratio $(l_c/r_v)^2 \sim 3$ is not large and ^{4}He only barely qualifies for the weak pinning limit. Thus, an observation of collective pinning would seem to require higher rotation velocities. Nevertheless, thermorotation measurements[60] up to 10 rad/s have suggested decreasing surface pinning with increasing vortex density. Thus, one should perhaps not exclude the possibility of observing collective surface pinning also in ^{4}He in the present experimental range of rotation velocities. In later experiments Tsakadze[61] increased the aspect ratio of his cell to $L/(2R) \leq 13$, which allowed him to identify from the slow vortex mode response also the elastic shear contribution from the vortex lattice in the bulk liquid, in a manner which is explained in Appendix D.

In view of the large vortex core size in ^{3}He-B it might become feasible to cover the top and bottom surfaces of the rotating container with an ordered lattice of pinning sites, prepared with microfabrication techniques. Collective unpinning of a vortex lattice from a commensurate lattice of pinning sites would then pose an interesting experimental task to observe. Perhaps such unpinning events might lead to sudden speedups in the rotation of a freely rotating light container. Presumably randomly occurring momentary rotation anomalies or glitches, followed by a slow relaxation recovery, might bear some relation to similar effects observed in the rotation decay of the fastest pulsars. Some calculations[62] and experiments[63] have suggested that a spindown of a freely rotating light container filled with superfluid ^{4}He might not be perfectly monotonous, but collective unpinning was not invoked in these cases.

VIII. CONCLUSIONS

In conclusion, we note that we have described both experimentally and theoretically two dynamic modes of quantized vortex lines in a vortex array under uniform rotation. These modes are a characteristic of any superfluid, but take different forms, depending on the hydrodynamic conditions. In the peculiar hydrodynamic environment of superfluid ^{3}He the motion of vortex lines in an array of vortices is always strongly overdamped: (1) a large-scale redistribution in vortex density involves the relatively fast mutual-friction-resisted motion, while (2) small deviations from equilibrium at nearly constant density are controlled by a slow vortex mode. The fast motion is impeded only by mutual friction, the weak surface pinning in ^{3}He is not involved. The measurements of the fast motion allow us to extract the dissipative part of mutual friction. The slow vortex mode, in turn, is governed by the elastic vortex line tension and collective weak surface pinning, which is manifested as reduced pinning at increasing vortex density. Collective pinning implies crystalline long-range order in the vortex array; the effective correlation length is found to be of order ten vortex lattice spacings.

Note added in proof. Further work on the phase-shift analysis in Appendix B 3 has removed some of the inadequencies listed in connection with Eq. (B3). In Ref. 71 we have proposed that the torque, which suppresses twisting and is proportional to vortex displacement (and thus to the time-dependent size of the vortex cluster), should be supplemented by a torque proportional to vortex velocity. The latter arises from the orientational influence of the superflow past the nonaxisymmetric vortex core in the perturbed vortex array. As a result $\Delta\varphi$ varies between 0 and 180° [instead of 0 and 90° in Eq. (B3)] and a more satisfactory fit to the experimental data in Figs. 24 and 25 is obtained, using for τ_F values from the independent measurement on the fast mutual-friction-resisted mode in Fig. 10.

ACKNOWLEDGMENTS

The mechanism of coupling between the spin absorption and the rotation of the nonaxisymmetric vortex was worked out[16] in collaboration with V. V. Dmitriev, Yu. M. Mukharsky, and G. E. Volovik. We are most grateful for this collaboration. For the experimental interpretation of the exponentially relaxing HPD signal, the critical velocity measurements[21] were of vital importance; we thank Ü. Parts for his responsibility there. We are indebted to P. J. Hakonen, J.P. Pekola, and E. V. Thuneberg for numerous discussions and to O. V. Lounasmaa for critical comments and interest in this work. This work was supported by the Körber Stiftung and through the ROTA cooperation plan of the Finnish Academy and the Russian Academy of Sciences.

APPENDIX A: HPD ABSORPTION MECHANISM FOR NONAXISYMMETRIC VORTICES

Here we discuss the mechanism, which couples the HPD absorption to vortex motion and is responsible for the exponentially relaxing component of the signal response ΔP_v in Fig. 9 (Sec. IV E). The mechanism has been described in Ref. 16 in the context of an isolated double-core vortex and is schematically reproduced in Fig. 19.

There exist two different singular vortex-core structures in the B phase: the axisymmetric core at high temperatures and high pressures, in a region bordering to the A phase in the pressure vs temperature phase diagram, and the nonaxisymmetric "double-core" at low temperatures. At the first-order phase transition from the axisymmetric vortex to the asymmetric vortex at $T = T_v(p)$, the HPD absorption increases discontinuously by a factor of 3. The jump is caused by a new dissipation mechanism, which is a direct consequence from the broken cylindrical symmetry of the core, and arises from the weak spin-orbit coupling between the orbital nonuniformity in the core and the coherently precessing spin magnetization. The spin precession forces the nonsymmetric core orientation in rapid rocking oscillation at twice the Larmor frequency. The oscillation of the nonaxisymmetric core cross section in the xy plane is resisted by mutual friction. It accounts for $\approx \frac{2}{3}$ of the total HPD absorption loss from these vortices.[16]

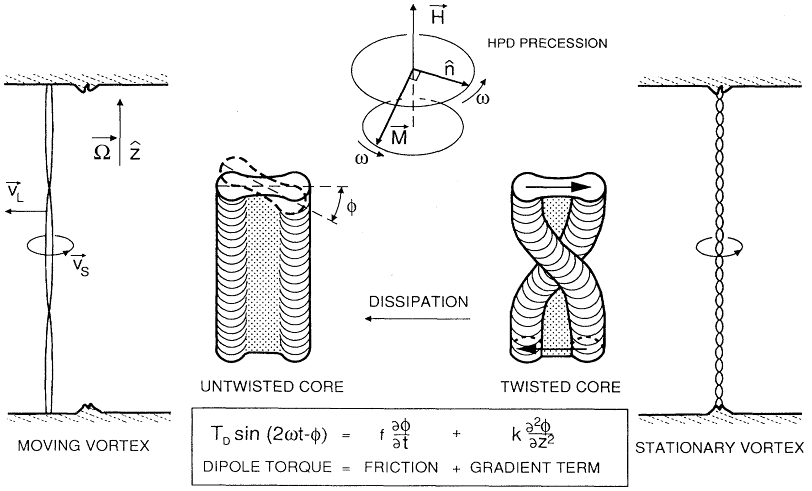

FIG. 19. Pictorial summary of the mechanisms involved in the HPD absorption of the nonaxisymmetric "double-core" vortex. The resonance losses originate from viscous dissipation, produced by the oscillation of the core cross section at twice the Larmor frequency at 2ω. This "rocking oscillation" is resisted by mutual friction [the damping coefficient $f \propto \rho_n B/(2\rho)$]. The amplitude of the oscillation is modulated by the amount of helical twisting of the core cross section along the axis. The pitch of the twisting and the absorption from the oscillation are at minimum when the vortex is stationary at constant Ω. When the vortex is in translational motion the pitch is increased, the amplitude of the rocking oscillation grows and leads to an increase in HPD absorption.

The average orientation in the *xy* plane, about which the core performs its rocking oscillation, is undetermined in an axisymmetric environment. A second consequence from the interaction with the coherent spin precession is a slow drift of the average core orientation in the direction of the precessing spins. The drift takes place on a time scale which is 2 orders of magnitude longer than the period of the Larmor precession.[16] The drift of the vortex-core orientation is resisted by a torque acting at the top and bottom walls at the pinned ends of the vortex line. It may be characterized as "rotational pinning," in contrast to a usual pinning force which resists translational motion. Rotational pinning and the slow drift will cause the core to become helically wound along its axis.

The winding increases the tension along the core due to the increase in gradient energy. The winding also partially restores cylindrical symmetry since, after averaging over the winding pitch, the orbital inhomogeneity of the twisted vortex core becomes less pronounced than in the untwisted state. For these reasons the mutual friction resisted dissipation from the 'rocking" oscillation of the core decreases when the vortex line becomes rotationally pinned i.e., when the core of the vortex becomes twisted. Conversely, when rotational pinning is weakened, the twisting uncoils and the absorption increases. A vestige from the uncoiling of the twisted cores is the initial increase in absorption in Fig. 6, following immediately after the reduction in Ω before any vortices have been expelled from the container. According to our numerical calculations with parameter values fitted to the experimental observations, the pitch in the twisting is ~ 0.4 mm and the time of its uncoiling is a few milliseconds. The equation used in this analysis is given in Fig. 19.

This picture is based on the broken cylindrical symmetry of the vortex core in the cylindrically symmetric surrounding. The cylindrical symmetry of the surrounding can be broken by tilting the magnetic field, by disturbing the equilibrium state of the vortex array, or by the interaction with image vortices in the vicinity of the cylindrical cell wall (Appendix B). If the cylindrical symmetry of the environment is broken, then a torque acts on the core and attempts to orient it. If the torque is weak, it suppresses twisting and the absorption increases. But a stronger torque will eventually suppress the "rocking" oscillation of the core and the absorption will then start to decrease. This twofold influence of the external torque is clearly displayed by the dependence of the absorption on the inclination angle η of the external field. The nonmonotonous η dependence of the NMR signal (see Ref. 16) provides the most convincing justification for our model of the absorption ΔP_v.

The single-vortex absorption model of the nonaxisymmetric vortex satisfactorily illustrates how the state of the vortex core influences the observed HPD absorption. However, a difficult problem is the coupling between the state of twisting of individual vortices and the motion in the vortex array, i.e., how the single-vortex absorption behavior is connected with the hydrodynamic eigenmodes of the vortex array and, in particular, its slowest mode. One possibility is that deformations of the vortex array during the slow vortex motion decrease symmetry and produce an additional weak torque acting on the double core. As discussed above, a weak torque suppresses twisting and increases the absorption. Another possibility is the interplay between the pinning in vortex translation and rotation. Different scales of roughness should be associated with these two types of pinning. Our estimate of the pining parameter b_s in Sec. VII D showed that a rather large roughness scale of order the intervortex distance accounts for the observed slow translational vortex motion. Roughness on such a scale is not able to pin the core rotation: only pinning sites of roughly the same size as the vortex core can be effective for rotational pinning. This means that during translation the ends of a vortex line move past a lot of rotational pinning sites. Then the pinning torque acting on the asymmetric vortex core randomly varies in time. One can expect that time averaging reduces this torque, in a similar manner as space averaging weakens the pinning force in collective pinning, i.e., rotational pinning is expected to be most effective when the vortex is at rest and settled to a fixed pinning site. A weaker pinning torque leads to weaker twisting and, as a result, to larger absorption. Thus, this model may explain why translational vortex motion triggers a HPD absorption increase.

The absorption response ΔP_v should be associated with an even power with respect to the effect of the external drive: twisting is at maximum when the vortex velocity and the vortex array deformation are zero, or the response does not depend on the sign of the deformation, as is shown by the experiment in Fig. 9. In the limit of small drive amplitudes $\Delta\Omega$ we assume that the response is quadratic, i.e., proportional to the square of the drive. In Fig. 9, one might then expect to observe a periodic component in ΔP_v, which would be a second or higher order even harmonic of the alternating component in the drive. However, if the phases of the second harmonic contributions from the different regions of the vortex array are incoherent, then the second harmonic is averaged out on the global scale. Therefore, the response ΔP_v is smooth, as is the case in Fig. 9, where no harmonic component can be distinguished within our experimental resolution.

APPENDIX B: VORTEX MOTION IN A HARMONIC ROTATION DRIVE

1. Amplitude dependences

Our analysis of the HPD resonance absorption is mainly concerned with its time dependence, but it is useful to point out a few features of the HPD amplitude behavior. In Fig. 20, the change in absorption level ΔP_v is plotted as a function of the modulation amplitude $\Delta\Omega$ of the harmonic component in the rotation drive. Here the increase in absorption ΔP_v refers to the difference between two stable states, the initial state at constant $\Omega=\Omega_0$ and the state when the harmonically modulated rotation drive has been acting for a sufficiently long time for all transients to die out. The number of vortices is the same for all measurements in this plot, while the average rotation velocity varies from 1.3 to 2.0 rad/s. The characteristic features of this plot are that a response at a measurable level exists at very small drive amplitudes (the data points in the extreme lower left corner of the plot have been recorded with $\Delta\Omega=0.0025$ rad/s) and that a saturated output level is eventually reached at drive amplitudes beyond $\Delta\Omega=0.05$ rad/s.

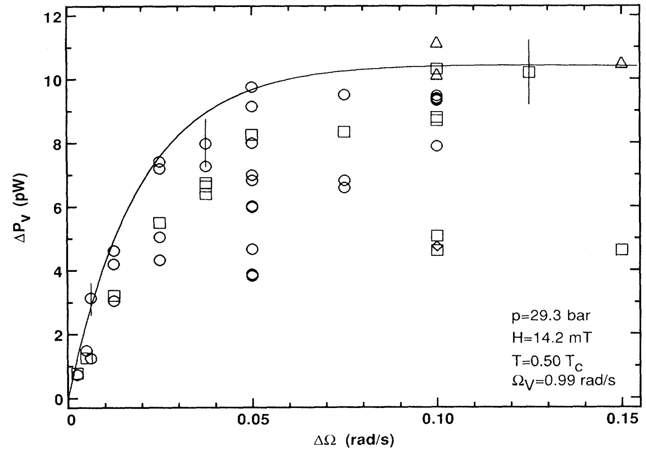

FIG. 20. The increase ΔP_v from the sinusoidally modulated rotation drive, plotted as a function of the amplitude $\Delta\Omega$ of the drive. Here ΔP_v represents the increase in absorption from the initial state at constant rotation Ω_0 to the state when the harmonic drive has acted sufficiently long to produce a steady output level. The number of vortices is kept constant and corresponds to the equilibrium state at $\Omega_v=0.99$ rad/s. The rotation drive $\Omega(t)=\Omega_0+\Delta\Omega(1-\cos\omega_m t)$ has a period $2\pi/\omega_m=30$ s and an average velocity Ω_0, which is 1.34 (circles), 1.69 (triangles), or 1.99 rad/s (squares). When the vortex cluster is first formed, a large ΔP_v value is measured for the virgin cluster and the result lies on the limit curve, which is approximated by the solid curve. If the measurement is repeated several times on the same cluster by switching on and off the harmonic component in the drive, ΔP_v may drop stepwise to lower levels, as shown by the data points below the limit curve. This drop in ΔP_v is well outside the measuring uncertainty, which is limited by the base line drift (Fig. 9) and is indicated by the vertical uncertainty bars.

However, Fig. 20 reveals additional details about the behavior of the HPD absorption contribution ΔP_v which can be characterized as follows: All data points, independent of the vortex density at which they have been measured, fall below the same envelope curve, which displays a steep initial rise and rapid saturation when $\Delta\Omega>0.05$ rad/s. The saturated absorption increase ΔP_v is found to be proportional to the number of vortices, independent of vortex density, and its value corresponds to $\approx 20\%$ of the total vortex absorption P_v.[16] A virgin vortex cluster, which has not been subject to Ω modulation, produces a response whose amplitude falls on the envelope curve. After having been repeatedly subject to a harmonic rotation drive the ΔP_v response drops below the envelope curve, which is illustrated by the many data points well below the envelope curve in Fig. 20: the response depends on the prehistory. Memory effects are typical for random systems, of which a system of surface pinning sites is an example. We believe that after repeated slow relaxations certain correlated regions in the vortex array find pinning sites, to which they are locked more effectively than other vortices on an average. In order to maximize the signal amplitude ΔP_v and to improve the resolution in the measurement of τ_s the slow vortex mode relaxation is recorded with a hydrodynamic drive which has been chosen to lie in the range of saturated response in Fig. 20, i.e., $\Delta\Omega=0.1$ rad/s has been used in most measurements.

The same change in absorption level ΔP_v, which in Fig. 20 is analyzed as a function of $\Delta\Omega$, is plotted in Fig. 21 as a function of ω_m. At low ω_m the response in ΔP_v is small, but it increases with increasing ω_m until it levels off at the saturated value of the envelope curve in Fig. 20. In Fig. 21, saturation starts at $\omega_m=1/\tau_{\rm sat}$. It is interesting to note that $\tau_{\rm sat}$ is close to the fast mode relaxation time $\tau_F \propto 1/(\Omega_0+\Delta\Omega)$, which depends on the average vortex density [see Eq. (7.22)] and was measured in the "rapid stop experiment" (Sec. VI). Two cases are shown in Fig. 21 for which this identification is quite well borne out (solid circles,, $\tau_{\rm sat}=5$ s vs $\tau_F=3$ s; open squares, $\tau_{\rm sat}=1.7$ s vs $\tau_F=1$ s). The vortex-density dependence of the saturation onset and of the absorption per one vortex below the saturation onset hints that the absorption mechanism is influenced by collective effects in the vortex array.

The motion excited by the harmonic drive can also be investigated from the properties of the HPD absorption signal in the equilibrium vortex state. In all previous measurements a metastable vortex cluster state has been

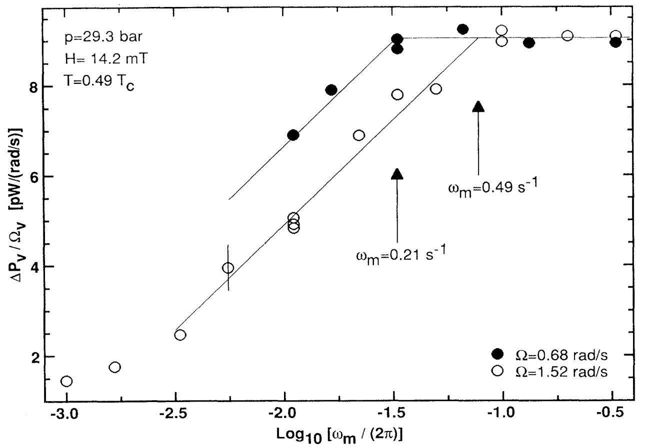

FIG. 21. The absorption increase ΔP_v plotted as a function of the frequency ω_m of the sinusoidally modulated rotation drive. On the vertical axis is the normalized absorption increase $\Delta P_v/\Omega_v$, where ΔP_v is defined as the increase in absorption from the initial state at Ω_0 to the steady-state value in the presence of the harmonic drive $\Omega(t)=\Omega_0+\Delta\Omega(1-\cos\omega_m t)$. On the horizontal axis is $\log_{10}[\omega_m/(2\pi)]$, where $\omega_m/(2\pi)$ is the frequency of the drive. Two cases are shown: ○, $\Omega_v=1.01$, $\Omega_0=1.52$ rad/s, and $\Delta\Omega=0.03$ rad/s; ●, $\Omega_v=\Omega_0=0.68$ rad/s and $\Delta\Omega=0.025$ rad/s. The onset for saturated response occurs at $\omega_m=1/\tau_{\text{sat}}$, indicated in both cases with vertical arrows. Since $\tau_{\text{sat}}\approx\tau_F$ and τ_F is inversely proportional to vortex density, i.e., $\tau_F \propto 1/(\Omega_0+\Delta\Omega)$ [see Eq. (7.22)], the region of saturated response starts at lower drive frequency for a vortex cluster of lower density.

studied, which is well isolated from interactions with the cylindrical cell wall by vortex-free counterflow. However, when the harmonic drive acts on an equilibrium state, the steady-state response incorporates a periodic absorption component at the frequency ω_m of the alternating drive, but phase shifted by $\Delta\varphi$. A measurement of $\Delta\varphi$ as a function of ω_m allows us to identify the time scale which characterizes the motion of the vortices in the presence of the alternating drive. This periodic component in the steady-state HPD absorption signal in the presence of the hydrodynamic drive is a second example of the coupling between the resonance amplitude and translational motion of vortices. The first example we encountered in the exponentially relaxing slow mode signal (Sec. IV E).

2. Equilibrium vs metastable vortex states: Differences in HPD signatures

The experimental basis for the harmonic component in the HPD absorption of the nonaxisymmetric vortex can be understood by inspecting Fig. 22. Suppose a vortex cluster is contracted from its equilibrium state to smaller size by accelerating Ω linearly. This measurement is shown for the axial field orientation $\eta=0$ in the top part of Fig. 22. The immediate response to the change in Ω is the increase in HPD absorption, when the vortices are set in motion and the winding of their cores is reduced. When the linear ramp in Ω is stopped, the exponentially relaxing signal from the slow vortex mode soon follows. These features were discussed in Sec. IV E. Of interest to us now is the fact that the final absorption level of the contracted cluster is larger than that in the equilibrium state: The absorption level P_v has increased by the amount $P_w\approx3.3$ pW in the contracted state at 1.68 rad/s compared to the equilibrium state at $\Omega_v=1.49$ rad/s. The increase P_w is 4% of the total absorption $P_v\approx79.3$ pW of the contracted cluster at constant Ω or, if phrased in a different form, it corresponds to half of the absorption from the vortices in the outermost ring.

A similar, but more monotonous and thus more readily measurable response is observed if the measurement is repeated with the magnetic field **H** tilted by more than the critical angle η_c from the axial orientation ($\eta_c\approx17°$ at $H=14.2$ mT). Then the twisting of the nonaxisymmetric vortex core is prevented by the torque provided from the coupling between **H** and the susceptibility anisotropy in the core. The absorption response in this situation is shown in the lower part of Fig. 22, where $\eta=20.4°$. Here the absorption increases during the linear acceleration of Ω until saturation is reached and the outermost vortices have been removed sufficiently far from the cylindrical wall to retrieve all of their absorption loss. This distance corresponds to an increase in the rotation velocity by $\Delta\Omega_w\approx0.14$ rad/s, when $\Omega_v=1.98$ rad/s. In more general terms we find that $\Delta\Omega_w\approx0.071\Omega_v$, in the conditions of Fig. 22, and that it is independent of the tilting angle η, when $\eta\geq\eta_c$. The measured $\Delta\Omega_w$ translates to a contraction $\Delta\approx\frac{1}{2}R\,\Delta\Omega_w/\Omega_v$ of the cluster radius R_v, which is thus independent of Ω_v and approximately 0.12 mm. For comparison the intervortex distance is 0.14 mm at $\Omega=1.98$ rad/s.

In an inclined field with $\eta=20.4°$ the increase in absorption is found to obey the dependence $P_w\approx-0.45+2.49\Omega_v$ pW at $T=0.48T_c$. In the same conditions the equivalent of the linear slope in Fig. 7 for the equilibrium state absorption was measured to be $dP_v/d\Omega_v=58.9$ pW s/rad. Thus, we find again that P_w is 4% of the total absorption of the contracted cluster. The same conclusion is reached from the measured tilting angle dependence of the absorptions: The absorption from the contracted cluster is observed to depend on η as $P_v(\eta)\approx8.19(1+8.66\cos^2\eta)$ pW and that of P_w is found to be $P_w\approx3.07\cos^2\eta$ pW (measured at $T=0.52T_c$ and $\Omega_v=1.48$ rad/s). The dependences of the different absorption components on η, T, and H have been briefly discussed in Ref. 16.

We conclude from these measurements that the absorption contribution P_w originates from the interaction of the vortex cluster with the cylindrical container wall. The interaction vanishes when the vortex cluster is contracted from its equilibrium state by a small constant amount which is comparable to one intervortex distance. The suppression of the absorption is 4% from the total absorption in the contracted cluster state, which means that the absorption of the peripheral vortices has dropped to $\frac{1}{2}$ from that of other vortices in the equilibrium state.

In summary we note that in a contracted cluster all vortices contribute an equal amount to the absorption while in the equilibrium state the peripheral vortices in-

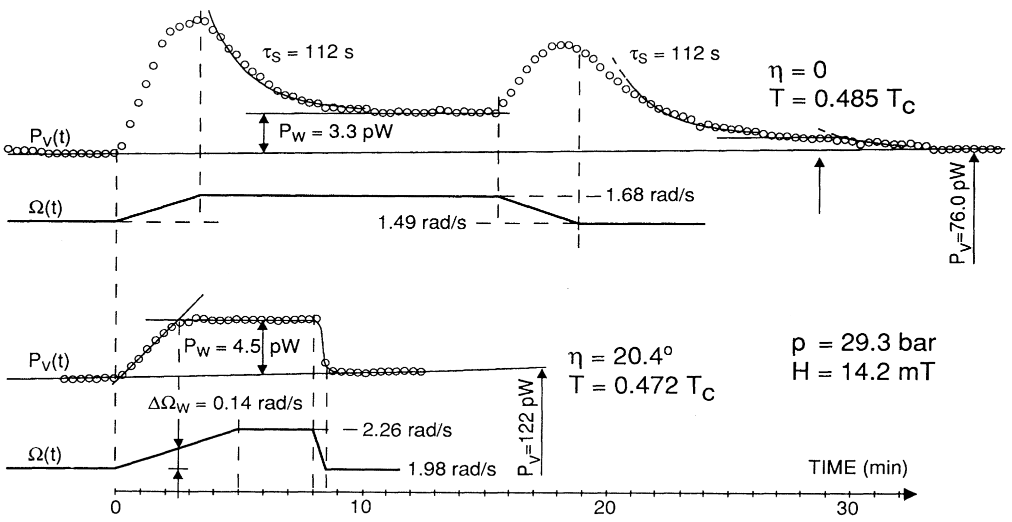

FIG. 22. HPD absorption level $P_v(t)$ in the equilibrium vortex state, where the outermost vortices interact with the cylindrical cell wall. P_v is monitored as a function of time while Ω is linearly increased from the equilibrium state and subsequently decelerated back to the equilibrium state. Top: *axial field* $\mathbf{H}\|\mathbf{\Omega}$. When the linear acceleration is started at $t=0$ from the equilibrium state $\Omega_v=1.49$ rad/s, the vortices are set in translational motion and the absorption level increases, similar to the response to the sinusoidal rotation drive in Fig. 9. When the acceleration is stopped at 1.68 rad/s and Ω is maintained constant, the slow mode relaxation soon starts. The difference from Fig. 9 is now that the contracted cluster at 1.68 rad/s has an absorption level which is higher by $\Delta P_w=3.3$ pW than that of the equilibrium state at 1.49 rad/s. During the deceleration back to the equilibrium state the same behavior is repeated and the absorption returns to its previous value in the equilibrium state (which is $P_v=76.0$ pW). In this second case the slow mode relaxation is anomalously long; the relaxation is restarted with a small amplitude when the peripheral vortices start interacting with the wall. Bottom: *tilted field*, $\mathbf{H}$ is inclined from $\mathbf{\Omega}$ by $\eta=20.4° > \eta_c$. When accelerating from the equilibrium state at $\Omega_v=1.98$ rad/s the absorption increases linearly until $\Omega=\Omega_v+\Delta\Omega_w=1.98+0.14=2.12$ rad/s and then remains constant during further acceleration. The increase in absorption $\Delta P_w=4.5$ pW represents approximately 4% of the equilibrium state absorption $P_v=122$ pW and corresponds roughly to one-half of the absorption of the outermost ring of vortices. We assume that all vortices contribute equally to the absorption when $\Omega \geq \Omega_v+\Delta\Omega_w$ (Sec. IV C).

teract with the image vortices associated with the cylindrical wall. This interaction imposes a torque on the peripheral vortices, suppresses their rocking oscillation, and thus reduces their absorption. In the presence of a harmonic rotation drive the small loss in absorption modulates the resonance absorption level when the outermost vortices travel in and out of the region, where their absorption depends on the distance from the cylinder wall. Again all magnetic relaxation effects are many orders of magnitude faster and therefore any lag between the drive and the absorption signal is entirely of hydrodynamic origin.

3. Equilibrium state response to harmonic rotation drive

The suppression of the viscous dissipation component in the HPD absorption near the cylindrical cell wall by the amount P_w is a small effect. Yet it is readily distinguishable in the measurement and can be used to study the motion of the peripheral vortices in the presence of a harmonic rotation drive. The measurement is illustrated in Fig. 23. The harmonic component in this absorption signal arises from the motion of the peripheral vortices into and out of the range of influence from the image vortices associated with the cylindrical wall. It is observed as a periodic loss and recovery of their dissipation by the amount $\Delta P_w \leq P_w$.

Figure 23 has been measured with a $2\pi/\omega_m=30$ s modulation period of the rotation drive. The absorption response displays a periodic component at the same frequency ω_m, but phase shifted by $\Delta\varphi$ from the drive. In the measured response minimum absorption corresponds to the minimum in the drive $\Omega(t)$, i.e., to the closest distance between the outermost vortices and the wall. This half-cycle of the harmonic response is always a sharp image of the drive while the second half-cycle corresponding to the contracted cluster is often a more fuzzy representation of a sinusoidal curve, if $2\Delta\Omega > \Delta\Omega_w$. The peak-to-peak value of the harmonic absorption component $2\Delta P_w$ is half of the P_w absorption contribution measured in Fig. 22. There are at least two reasons which explain this smaller value: (1) The peak-to-peak value of the drive amplitude $2\Delta\Omega=0.10$ rad/s is less than the required $\Delta\Omega_w=0.14$ rad/s to recover all of the absorption P_w (see lower part of Fig. 22). (2) The dynamic response at the modulation frequency $\omega_m=2\pi/30\ \mathrm{s}^{-1}$ is smaller than the dc response, i.e., the amplitude of the harmonic component in the response decreases with increasing ω_m. With a modulation period of 15 s, the harmonic response is still observable, but smaller than in Fig. 23. When the period of the modulation is reduced to 3 s the amplitude of the harmonic component becomes too small for an accurate measurement of $\Delta\varphi$.

In Fig. 23, with a 30-s period of the drive, the response is lagging behind by a phase shift $\Delta\varphi \approx 70°$. The phase shift $\Delta\varphi$, by which the drive leads the absorption

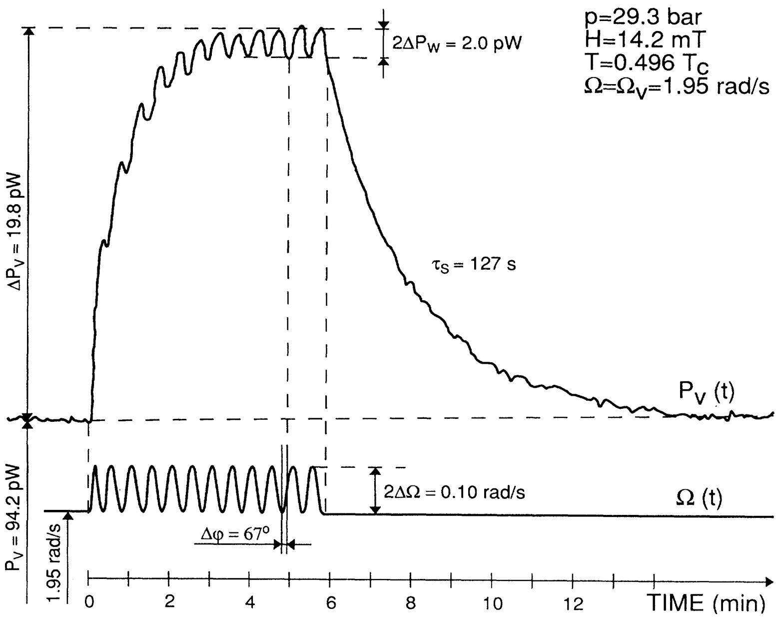

FIG. 23. Absorption response of the equilibrium vortex state to a sinusoidally modulated rotation drive. Bottom: Rotation velocity $\Omega(t)=1.95+0.05(1-\cos\omega_m t)$ rad/s, with $\omega_m=2\pi/30$ s^{-1}. Top: HPD absorption level ΔP_v as a function of time. In the equilibrium vortex state the periodic contraction and expansion of the vortex cluster produces a periodic contribution in the HPD absorption signal, where the principal component is at the fundamental drive frequency, but phase shifted by $\Delta\varphi$. The periodic response originates from the motion of the outermost vortices, when their absorption depends on the distance from the cylindrical container wall. Here the minimum of the rotation velocity $\Omega_{\min}$ corresponds to the minimum in absorption and to closest approach to the side wall; $\Omega_{\min}$ and the minimum of ΔP_w are used as reference points for measuring the phase shift $\Delta\varphi$.

response, when measured at the minimum Ω value ($\approx\Omega_v$) where the periodic response is most clearly defined, is a well-identifiable experimental observable. From the measurements we find it to depend on the vortex density $n_v\propto\Omega_v$ and the modulation frequency ω_m of the rotation drive. These dependences are shown in Figs. 24 and 25, respectively. In comparison, the dependence on the modulation amplitude $\Delta\Omega$ of the drive was found to be much weaker. The measurements in Figs. 24 and 25 have been performed on the equilibrium vortex state using a rotation drive $\Omega(t)=\Omega_v+\Delta\Omega(1-\cos\omega_m t)$, which is found to preserve the total number of vortices. The phase shift $\Delta\varphi$ is measured after the sinusoidal drive has been acting for a sufficiently long time to reach a steady-state response in absorption. This means that all transient time dependences have had a chance to decay and the measurements should be compared to a steady-state solution of the hydrodynamic equations.

For a qualitative description of the phase lag we simply associate the sinusoidal response in ΔP_w with the oscillating cluster radius $R_v(t)$. The maximum cluster size $R_v\approx R$ corresponds to the equilibrium state, where the peripheral vortices have lost roughly half of their absorption and the minimum signal amplitude in ΔP_w is recorded. When the cluster subsequently contracts towards its minimum size the absorption loss of the peripheral vortices is regained and the maximum signal in ΔP_w is observed. Since the number of vortices $N=\pi R_v^2(t)n_v(t)=$const, a small change ΔR_v in the cluster size drives a similar change in the vortex density $\Delta n_v\approx-2n_v^{\mathrm{eq}}\Delta R_v/R$, where n_v^{eq} is the density in the equilibrium state at Ω_v.

The vortex density $n_v(t)$ is controlled by Eq. (6.4) which was derived for a constant rotation velocity. We can take account of the harmonic component in $\Omega(t)$ by enforcing a small-amplitude oscillation in the normal

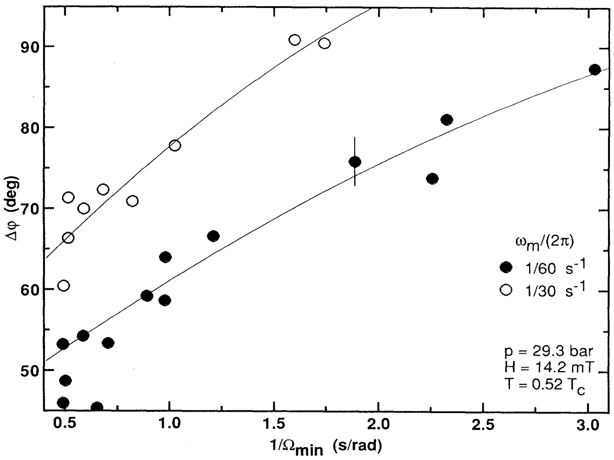

FIG. 24. Measurement of the phase shift $\Delta\varphi$ between the sinusoidally modulated rotation drive and the absorption contribution ΔP_w close to the equilibrium state. Here $\Delta\varphi$ is plotted as a function of the inverse vortex density at the closest approach to the cylindrical wall, which is $\propto 1/\Omega_{\min}$. The results pertain to the steady-state situation, where the harmonic component in the drive has been acting sufficiently long to produce a stable value for $\Delta\varphi$. The solid lines are fitting curves $\Delta\varphi=\Delta_0\varphi+(180°/\pi)\arctan(A/\Omega_{\min})$ which differ from Eq. (B3) by a constant shift $\Delta_0\varphi$. Two modulation frequencies $\omega_m/(2\pi)$ of the drive are shown: the open circles correspond to modulation with a period of 30 s and are fitted by $\Delta_0\varphi=53°$ and $A=0.45$ rad/s. In terms of Eq. (B3); it would correspond to a mutual friction coefficient $B\rho_n/\rho=0.5$. The solid circles are for a modulation period of 60 s and their least-squares fit gives $\Delta_0\varphi=44°$ and $A=0.31$ rad/s, which translates to $B\rho_n/\rho=0.3$. The amplitude $\Delta\Omega$ of modulation in the rotation drive is 0.03–0.05 rad/s; its value does not affect the phase shift in first order.

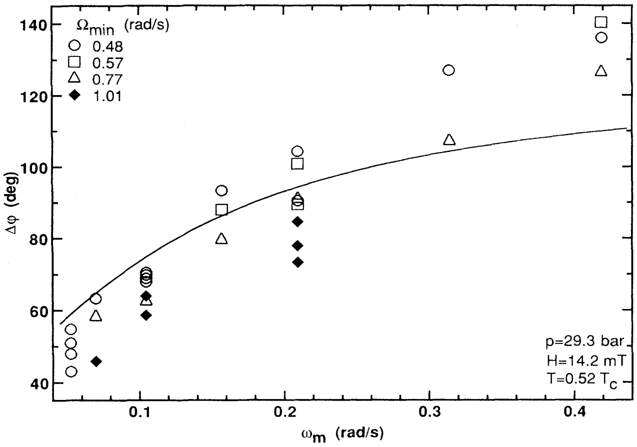

FIG. 25. Measurement of the phase shift $\Delta\varphi$ between the sinusoidally modulated rotation drive and its absorption response ΔP_w close to the equilibrium state. Here $\Delta\varphi$ is plotted as a function of the drive frequency $\omega_m/(2\pi)$. The different symbols refer to different vortex densities, which are specified by the minimum value Ω_{min} of the rotation drive, where $\Omega_{min} \approx \Omega_v$. The solid curve is a fit to the open circles with $\Omega_{min}=0.48$ rad/s and $\Delta\varphi = 39° + (180°/\pi)\arctan(6.8\omega_m)$, which gives $B\rho_n/\rho = 0.3$. The amplitude of the modulation in the rotation drive is $\Delta\Omega = 0.10$ rad/s, except for the data denoted with open squares, which have been recorded with $\Omega_{min}=0.57$ rad/s and $\Delta\Omega = 0.05$ rad/s.

component of Eq. (5.4): it plays the role of an external force if we set $\mathbf{v}_n = \Delta\Omega[\hat{\mathbf{z}}\times\mathbf{r}](1-\cos\omega_m t)$. We then obtain the equation of motion for the vortex density, namely, Eq. (6.4),

$$\frac{d\Omega_s}{dt} + \frac{\rho_n}{\rho} B\Omega_s[\Omega_s - \Omega(t)] = 0 , \tag{B1}$$

where $\Omega_s = \kappa n_v(t)/2$ and $\Omega(t)$ is the time-dependent rotation drive expressed in the laboratory frame. In linearized form Eq. (B1) reads

$$\frac{d\Delta n_v}{dt} + \frac{\Delta n_v}{\tau_F} = \frac{2\Delta\Omega}{\tau_F \kappa}(1-\cos\omega_m t) , \tag{B2}$$

where $\tau_F = (B\Omega\rho_n/\rho)^{-1}$ is the decay time of the fast mode. A naive approach is to equate the phase shift $\Delta\varphi$, by which the drive $\Omega(t)$ leads the absorption response $\Delta P_w(t)$, with the phase shift between $\Omega(t)$ and the cluster radius $R_v(t)$, i.e., Δn_v. This gives a phase shift

$$\Delta\varphi = \arctan\omega_m \tau_F . \tag{B3}$$

This procedure assumes that mainly the fast mode contributes to the response and determines the phase lag. It displays some qualitative features of the dependences in Figs. 24 and 25: it increases as n_v^{eq} decreases and ω_m increases. However, there remain discrepancies: (i) the calculated $\Delta\varphi$ lies a constant shift of ~40° lower in value; (ii) the measured values are so high that they exceed 90°, which is unphysical for an overdamped mode. These differences reflect the fact that not only the fast mode contributes to the phase lag of the response, but it is a superposition of the fast and the slow modes. Furthermore, the phase lag is associated with the motion of peripheral vortices, i.e., $\Delta\varphi$ should be analyzed as a local rather than a global phase shift. Nevertheless, this simplified analysis of phase lags confirms that the motion in the presence of the harmonic rotation drive is essentially driven by the fast mutual-friction-resisted mode. (See note added in proof.)

APPENDIX C: PINNING AT SUPERFLUID INTERFACES: ^{3}He-*B* ABOVE ^{3}He-^{4}He SOLUTION

Interactions between vortices and different boundaries is an intriguing testing ground for probing the structure and dynamics of vortices. At solid surfaces the influence of surface roughness is expected to be an important component in pinning. Different types of phase boundaries can also be introduced in the rotating container and are expected to raise new questions. At the free surface of the liquid, bordering to the vapor phase, no pinning is expected, but a vortex still bends the interface creating a shallow dimple of ~10-Å depth where the core intercepts the surface.[64] At the phase boundary between concentrated ^{3}He-*B* and the 6.4% solution of ^{3}He in superfluid ^{4}He, the influence of vortices in both phases is expected to be more serious on the interface profile.[65] Finally, at the first-order phase boundary, separating the *A* and *B* phases of superfluid ^{3}He vortices are expected to be interlocked.[66]

Measurements on pinning with different kinds of solid surfaces are time consuming. Therefore, one might speculate that a simple alternative to vary the pinning characteristics might be to include ^{4}He in the rotating container. If a small proportion of ^{4}He is added, the solid surfaces become coated with a superfluid ^{4}He film at pressures below 25 bars, the solidification pressure of ^{4}He. (At higher pressures the surface structure will presumably depend on the temperature and the rate at which the solidification point is exceeded. This case will not be considered here.) It is not clear what effect a thin superfluid lining of ≤300-Å thickness would have on pinning. It is possible that the central part of the ^{3}He-*B* vortex will penetrate through the film and maintain contact with the solid wall, thereby effectively making it possible to trap a circulation also in the ^{4}He film around the ^{3}He vortex core. This possibility is suggested by studies on vortices in pure superfluid ^{4}He films.[67]

When the proportion of ^{4}He is further increased in the sample chamber then the bulk 6.4% ^{3}He-^{4}He mixture phase is precipitated on the bottom. The solid surfaces above the phase boundary are covered with a saturated superfluid ^{4}He film which contains dissolved normal ^{3}He with a concentration gradient perpendicular to the wall. Eventually, if one continues replacing ^{3}He with more ^{4}He, the phase boundary separating the bulk phases is raised inside the NMR cell, providing now a lower pinning surface for the ^{3}He-*B* vortices above the interface. The top surface of the NMR cell is coated with the saturated superfluid ^{4}He film. In this case one might expect τ_s to increase by a factor of 2, if pinning at the interface between the bulk phases approaches that at the free surface of a superfluid, namely, is absent altogether.

We have performed measurements on the exponential relaxation time τ_s of the slow vortex mode in three different situations at 23.5-bars pressure: (1) The reference case is obtained with pure ^{3}He. In addition two different concentrations of ^{3}He-^{4}He mixture were used such that in one case (2) the phase boundary is well below the NMR cell while in (3) the second case it is inside. The conclusion from these measurements is that within the present experimental resolution no conclusive increase in τ_s could be established in cases (2) and (3). This means that neither a superfluid ^{4}He film coating nor the interface to a bulk ^{3}He-^{4}He mixture phase change the pinning of the ^{3}He-B vortices by more than 40% from the value measured for the epoxy surface with pure ^{3}He.

In fact, it may not be so surprising that pinning is not absent at the interface between the two bulk superfluids and is thus stronger than at the free surface. The dimples formed by the ^{4}He and ^{3}He vortices from both sides of the interface should interact which results in a coupling of their motions. This coupling may be rather intricate, since the vortex densities on the two sides of the interface are related as $n_3{:}n_4=\kappa_4{:}\kappa_3=3{:}2$ and thus the vortex lattices are incommensurate.[50]

A more exact characterization of pinning at the interface between the bulk phases of ^{3}He-B and the ^{3}He-^{4}He solution awaits measurements with improved resolution. An additional bonus of such measurements is that they provide a means to study the dependence of τ_s on the height L of the ^{3}He-B layer by repeating the measurements with the phase boundary at different heights. With our present signal resolution it is not feasible to perform measurements on the slow vortex mode in the presence of a free surface at zero pressure.

APPENDIX D: BULK CRYSTALLINE EFFECTS OF A VORTEX ARRAY

The slow collective mode, which we have observed, is governed by the elastic tension of vortex lines and weak surface pinning. Shear elasticity is important only within the Ekman layers. On the other hand, the original motivation for studying the slow vortex motion was to find the Tkachenko wave, which arises from the shear elasticity of the vortex lattice in the bulk liquid.[28] Let us now analyze the effect of the bulk shear rigidity on the slow vortex mode.

Shear deformations induce a velocity field around a vortex line in addition to that due to bending deformations. Then Eq. (7.2) is replaced by[13]

$$\mathbf{v}_{sl}=\mathbf{v}_s+\nu_s\left[\hat{\mathbf{z}}\times\frac{d^2\mathbf{u}}{dz^2}\right]+\frac{c_T^2}{2\Omega}\{\hat{\mathbf{z}}\times[\Delta\mathbf{u}-2\nabla(\nabla\cdot\mathbf{u})]\}\ . \tag{D1}$$

Here ∇ and Δ are operations in the xy plane and c_T is the Tkachenko wave velocity for a triangular vortex lattice given by

$$c_T^2=\frac{\kappa\Omega}{8\pi}\ . \tag{D2}$$

By repeating the derivation for the plane-wave solution $\sim\exp(i\mathbf{q}\cdot\mathbf{r}-i\omega t)$ given in Sec. VII C, one obtains the previous dispersion equation Eq. (7.24) for the frequency ω of the slow vortex mode, but now the elastic frequency ω_Σ is given by [cf. Eq. (7.20)]

$$\omega_\Sigma=\frac{2\nu_s}{L}b+\frac{c_T^2q^2}{2\Omega}=\frac{2\nu_s}{L}b+\frac{\kappa q^2}{16\pi}\ , \tag{D3}$$

when the viscous surface force $\propto b_1$ is neglected.[50] Equation (D3) incorporates the elastic effects both from line-tension and pinning (the first term $\propto b$) and from the Tkachenko rigidity (the second term $\propto c_T^2$). The wave number q in the Tkachenko term is determined from the conditions on the vertical border of the vortex cluster. For the sake of simplicity we analyze the problem of the elastic shear contribution to the slow mode in the absence of surface pinning, when all motion is restricted to the xy plane. Then the relaxation time of the slow vortex mode is given by

$$\frac{1}{\tau_T}=i\omega=\frac{c_T^2q^2}{2\Omega\beta}=\frac{\kappa q^2}{16\pi\beta}\ . \tag{D4}$$

This spectrum resembles that of a viscous mode; however, the circulation quantum κ rather than the kinematic viscosity ν enters this expression. The relaxation time of this mode is inversely proportional to the shear rigidity of the vortex crystal [the factors in Eq. (D4) represent the Tkachenko rigidity of the triangular lattice], and the existence of such a mode is a signature of crystalline order in the vortex array. Comparing the vortex crystal with a usual crystal made of atoms, one would expect exponentially relaxing motion if one were to assume the atoms to be immersed in a viscous fluid. Then the transverse sound mode for such a crystal would transform to a viscously damped mode with the imaginary frequency proportional to shear rigidity.

According to the correspondence principle, the spectrum in Eq. (D4) relates to a differential equation of the type of a diffusion equation describing the slow mode in space and time:

$$\beta\frac{\partial\Psi}{\partial t}+\frac{\kappa}{16\pi}\Delta\Psi=0\ . \tag{D5}$$

Here Δ is the Laplacian in the xy plane and the vector potential $\boldsymbol{\Psi}$ determines the field of the vortex displacements $\mathbf{u}=\nabla\times\boldsymbol{\Psi}$ satisfying the incompressibility condition $\nabla\cdot\mathbf{u}=0$. Here we consider axisymmetric oscillations, with the displacement vectors $\mathbf{u}$ confined to the xy plane. Then the potential $\boldsymbol{\Psi}=\Psi\hat{\mathbf{z}}$ and in the cylindrical coordinate frame (r,φ) the displacement $\mathbf{u}$ has only the azimuthal component $u=-\partial\Psi/\partial r$ which does not depend on the azimuthal angle φ.

One should supplement Eq. (D5) by the boundary condition at the border $r=R_v$ of the vortex crystal of radius R_v. In deriving the boundary condition, Ruderman[68] assumed free rotation of a very light container, imposing conservation of the angular momentum of the superfluid in the container. Then the transverse component of the stress tensor of the vortex crystal,

$$\sigma_{r\varphi}=-\rho_s c_T^2\left[\frac{\partial u}{\partial r}-\frac{u}{r}\right]\ , \tag{D6}$$

vanishes at $r=R_v$. The opposite simple limit is a fixed boundary of the vortex crystal, when $u=0$ at $r=R_v$. This boundary condition was proposed by Williams and Fetter.[69] Here we consider a more general condition for the case when the vortex crystal interacts with the container wall and the latter is able to move independently. Then the momentum flux through the boundary of the vortex crystal given by the stress-tensor component $\sigma_{r\varphi}$ is balanced by the force from the wall:

$$-\sigma_{r\varphi}=-k(u-w)-\eta\left[\frac{\partial u}{\partial t}-\frac{\partial w}{\partial t}\right] . \tag{D7}$$

Here w is the azimuthal linear displacement of the wall, k is the parameter of the elastic force, and η is the coefficient of friction between the vortex crystal and the container wall.

The elastic force proportional to k can appear only if cylindrical symmetry is broken (because of ellipticity of the container, for example). However, a symmetry-breaking interaction with the wall is assumed weak so that the problem remains axisymmetric. The frictional force between the vortex crystal and the wall is possible because of direct interaction of vortices with the rough surface of the wall or by means of the normal component if the latter participates in the oscillation (see Sec. VIII D in Ref. 13).

We also need the equation of motion for the container. For the free rotation of the container, if it interacts only with the superfluid, the equation is

$$I\frac{d^2w}{dt^2}=-2\pi R^3L\left[k(w-u)+\eta\left[\frac{\partial w}{\partial t}-\frac{\partial u}{\partial t}\right]\right] . \tag{D8}$$

Here I is the moment of inertia and L is the height of the container of radius R.

Equations (D5)–(D8) determine the modes of our resonator. Axisymmetric modes correspond to a cylindrical wave

$$\begin{aligned}\Psi&=\Psi_0 J_0(qr)\exp(-i\omega t) ,\\ u&=-\frac{\partial\Psi}{\partial r}=\Psi_0 qJ_1(qr)\exp(-i\omega t) ,\end{aligned} \tag{D9}$$

with the wave number q related to the frequency ω in Eq. (D4). Substituting Eq. (D9) into the boundary condition Eq. (D7) and the equation of motion Eq. (D8) where $w=w_0\exp(-i\omega t)$, then upon excluding w, one obtains the following equation determining the wave numbers q for the eigenmodes of the resonator:

$$\rho_s c_T^2 q^2 J_2(qR_v)=\frac{\omega^2 I(k-i\omega\eta)}{\omega^2 I-2\pi R_v^3 L(k-i\omega\eta)}qJ_1(qR_v) . \tag{D10}$$

For a very light container ($I=0$) Eq. (D10) yields Ruderman's wave numbers for the oscillations of the free vortex crystal determined from the equation $J_2(qR_v)=0$:

$$q_R(s)=\frac{j_{2,s}}{R_v} . \tag{D11}$$

Here $j_{n,s}$ denotes the sth zero of the Bessel function $J_n(x)$. According to Ruderman, the fundamental eigenfrequency corresponds to $j_{2,1}=5.14$. The Williams-Fetter boundary condition, $u=0$ at $r=R_v$, is obtained from Eq. (D10) assuming $I\rightarrow\infty$ and $|k-i\omega\eta|\rightarrow\infty$ (a very heavy container and strong coupling of the vortex crystal with the wall). Now the wave numbers are determined from the equation $J_1(qR_v)=0$:

$$q_{\mathrm{WF}}(s)=\frac{j_{1,s}}{R_v} . \tag{D12}$$

The fundamental eigenmode with the lowest frequency corresponds to the smallest root $j_{1,1}=3.83$. From these estimates it looks as if the wave number for the fundamental eigenmode in the cylindrical resonator cannot be lower than $3.83/R_v$. However, numerical calculations by Campbell[70] have yielded that there exist eigenmodes for the vortex pattern with a fixed outermost ring of vortices, for which the wave numbers are a factor of 2 lower than this value. This controversy has been discussed in Ref. 13. In fact, the Ruderman wave number $q_R(1)=5.14/R_v$ is not the lowest one for the free-vortex crystal. The spectrum also includes one mode at zero frequency, corresponding to the Goldstone mode due to the invariance in rotating the vortex crystal with respect to the container. When rotational invariance is broken because of interaction with the wall, the zero-frequency mode becomes an observable mode with finite frequency, which may be arbitrarily low (a soft rotational mode). In the numerical calculation of Campbell,[70] the fixed outermost ring of vortices imitated the role of the wall.

Thus, the wave number for the fundamental eigenmode of the vortex crystal should be determined from the spectrum given by Eq. (D10), taking into account interactions with the wall. Assuming that the wave number q is small compared to $1/R_v$, one can expand the Bessel functions. Then the equation for the eigenfrequency of the soft rotational mode becomes

$$\frac{\rho_s R_v\Omega\beta}{2}[\omega^2 I-2\pi R_v^3 L(k-i\omega\eta)]=-i\omega I(k-i\omega\eta) . \tag{D13}$$

Our experimental conditions correspond to the limit of a very heavy container ($I\rightarrow\infty$). Then the fundamental eigenfrequency is given by

$$\omega_0=\frac{-2ki}{\rho_s R_v\Omega\beta+2\eta} . \tag{D14}$$

Thus, a weak symmetry-breaking elastic interaction with the wall may be responsible for a very low fundamental eigenfrequency proportional to the interaction strength k. However, this eigenfrequency increases if the container becomes lighter (I decreases). Then the fundamental eigenfrequency is (viscous interaction is neglected, $\eta=0$)

$$\omega_0=\sqrt{2\pi R_v^2 Lk/I} . \tag{D15}$$

One may use these expressions as long as the absolute value of the wave number $|q|=4\sqrt{\pi\beta|\omega_0|/\kappa}$ is small compared to the Ruderman wave number $5.18/R_v$. Otherwise the fundamental eigenfrequency is determined by the Ruderman wave number, as follows from a more general dispersion equation [Eq. (D10)] in the limit $I \rightarrow 0$, independently of the type and amplitude of interaction between the vortex crystal and the container wall. It is difficult to approach this limit if the symmetry-breaking interaction is weak.

Bearing in mind this analysis, we can now compare the experimental conditions for the observation of the Tkachenko contribution in the experiment by Tsakadze in ^{4}He (Ref. 61) and in our case in ^{3}He-*B*. The difference is as follows.

(1) Tsakadze[61] has observed oscillations of a freely rotating light container with a moment of inertia not larger than that of the superfluid. In contrast, in our experiment the container is rigidly connected to the rotating cryostat. This case corresponds to a very heavy container with $I \rightarrow \infty$.

(2) In ^{4}He the vortex crystal is coupled with the wall by means of the normal component. The normal component is dragged along by the oscillating vortices and it also sticks to the wall; it provides a considerable frictional force between the vortex crystal and the wall. In ^{3}He the normal component does not participate in the motion of vortices (clamped regime) and this mechanism does not work. The only coupling is provided by weak deviations from cylindrical symmetry.

This explains why the fundamental eigenfrequency should be of the order of the Ruderman frequency in the measurements of Ref. 61, but is expected to be much lower in our experiment. In any case, q depends on $R_v \propto \sqrt{\Omega_v/\Omega}$. Thus, the Tkachenko term depends on Ω, if it is measured at fixed N_v, while it is independent of Ω if R_v is kept constant (since it results from a competition between the elastic force per unit volume $[\approx n_v(v_{sl}-v_s)]$ and the mutual friction force $[\approx n_v B v_L]$, both $\propto \Omega$).

By measuring τ_s as a function of Ω_v while Ω is kept constant, one should be able to isolate the Tkachenko contribution. Results from such measurements are shown in Figs. 26 and 27. In Fig. 26, one can compare the relaxation of the slow mode signal at different values of Ω_v and in Fig. 27 the time τ_s as a function of Ω_v is shown: here the ratio Ω/Ω_v varies from 1 to 5 but τ_s remains constant, within the resolution of ±30 s in the time constant determination in this collection of data. A more stringent test with a ±10-s resolution is examined in Fig. 26 and arrives at the same conclusion. We thus find that the Tkachenko term is too small to be distinguishable within the precision of $\approx \pm 10$ s of our τ_s measurement. If we were to assume vanishing momentum flux across the vortex-crystal boundary (the Ruderman condition), one then would obtain $q = 5.18/R_v$. The Tkachenko term in Eq. (D3) becomes

$$c_T^2 q^2/2\Omega = 0.52\kappa/R_v^2 \approx 3\times 10^{-3}\Omega/\Omega_v \ \mathrm{s}^{-1}$$

and a clearly distinguishable positive slope would be visible in Fig. 27. As was discussed above, in a massive sample container a soft mode with a smaller q is also possible. The absence of the Tkachenko contribution we thus interpret to mean that a rotational soft mode with very

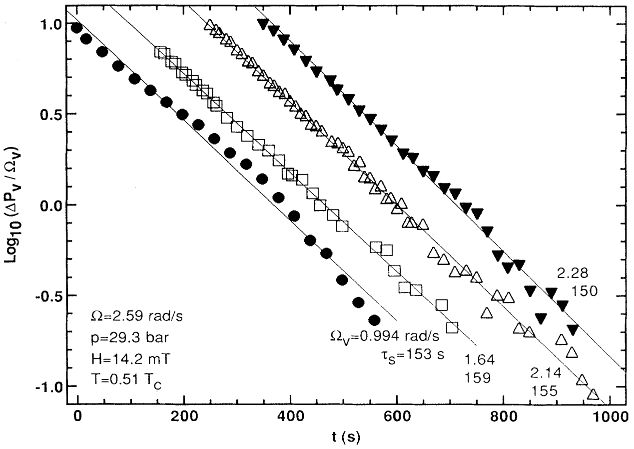

FIG. 26. Demonstration of the independence of τ_s on the size of the vortex cluster. This plot is similar to Fig. 16 and shows four sets of measurements on the exponential relaxation time τ_s, which have been plotted in terms of $\log_{10}(\Delta P_v/\Omega_v)$ as a function of time. All four measurements have been performed in as similar conditions as possible and give $\tau_s = 150-159$ s with a relative precision, which is better than ±10 s. The actual rotation velocity is kept constant at $\Omega = 2.59$ rad/s while Ω_v is varied from 0.994 to 2.28 rad/s. The conclusion from this comparison is that within the present measuring resolution τ_s does not depend on Ω_v and the radius $R_v = R\sqrt{\Omega_v/\Omega}$ of the vortex cluster. On the vertical axis is the normalized absorption component ΔP_v (in pW). On the horizontal axis the zero point corresponds to the moment when the harmonic drive is switched off. For three of the relaxation decays the zero has been shifted by 150 s (squares), 250 s (open triangles), and 350 s (solid triangles).

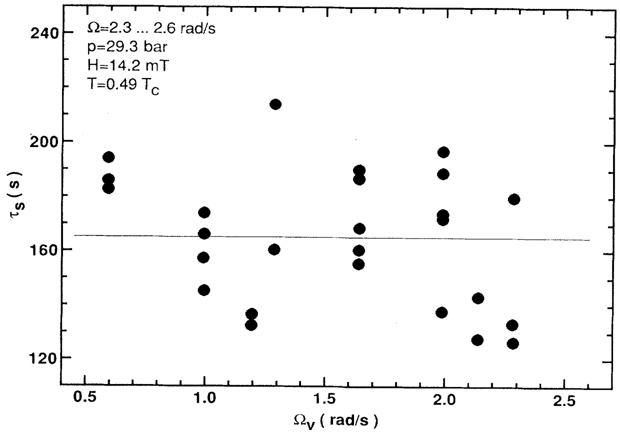

FIG. 27. Measurement of the dependence of the time constant τ_s on the number of vortices $N_v \propto \Omega_v$, i.e., the radius $R_v = R\sqrt{\Omega_v/\Omega}$ of the vortex cluster. The measurements have been performed at roughly constant Ω and are plotted as a function of Ω_v. The result does not reveal a dependence within the overall experimental uncertainty of ±30 s of one τ_s measurement. This result justifies the conclusion that the contribution from the shear elasticity of the vortex array in the bulk liquid is not present in the slow mode response.

small q is excited. This also means that the only vortex-crystal mechanism, which is observed to contribute to the slow relaxation, is the effect from the shear rigidity in the Ekman layer on surface pinning.

In summary, the absence of any observable contribution from bulk deformations (outside the Ekman layers) of the vortex lattice in the transverse xy-plane means that the observed slow relaxation involves a rotational soft mode of the whole vortex cluster with very small value of q. To improve the sensitivity in detecting this vortex lattice term one should substantially increase either the ratio Ω/Ω_v or L/R, all of which is being planned.

---

[*] Present address: Physics Department, University of Bayreuth, 8580 Bayreuth, Germany.

[†] Permanent address: Ioffe Physical Technical Institute, 194021 St. Petersburg, Russia.

[1] R. J. Donnelly, *Quantized Vortices in Helium* (Cambridge University Press, Cambridge, 1991).

[2] D. R. Tilley and J. Tilley, *Superfluidity and Superconductivity* (IOP, Bristol, 1990).

[3] D. Vollhardt and P. Wolfle, *The Superfluid Phases of Helium-3* (Taylor and Francis, London, 1990).

[4] Experimental review on vortices in ^{3}He superfluids: P. Hakonen, O. V. Lounasmaa, and J. Simola, Physica B **160**, 1 (1989).

[5] Theoretical review on vortices in ^{3}He superfluids: M. M. Salomaa and G. E. Volovik, Rev. Mod. Phys. **59**, 533 (1987).

[6] J. A. Sauls, in *Timing Neutron Stars*, Vol. 262 of NATO Advanced Study Institute, edited by H. Ögelman and E. P. van den Heuvel (Kluwer Academic, Dordrecht, Holland, 1989), p. 457.

[7] G. Baym, R.I. Epstein, and B. Link, Physica B **178**, 1 (1992).

[8] A. G. Lyne and F. Graham-Smith, *Pulsar Astronomy* (Cambridge University Press, Cambridge, 1990).

[9] W. F. Vinen, Proc. R. Soc. London Ser. A **260**, 218 (1961); S. C. Whitmore and W. Zimmermann, Jr., Phys. Rev. **166**, 181 (1968); P. W. Karn, D. R. Starks, and W. Zimmermann, Jr., Phys. Rev. B **21**, 1797 (1980).

[10] J. C. Davis, J. D. Close, R. Zieve, and R. E. Packard, Phys. Rev. Lett. **66**, 329 (1991).

[11] W. I. Glaberson and R. J. Donnelly, in *Progress in Low Temperature Physics*, edited by D. F. Brewer (Elsevier-North-Holland, Amsterdam, 1986), Vol. 9, p. 1.

[12] B. Baym and E. Chandler, J. Low Temp. Phys. **50**, 57 (1983); **62**, 119 (1986).

[13] E. B. Sonin, Rev. Mod. Phys. **59**, 87 (1987).

[14] E. B. Sonin, Y. Kondo, J. S. Korhonen, and M.Krusius, Europhys. Lett. **22**, 125 (1993).

[15] A. S. Borovik-Romanov, Yu. M. Bunkov, V. V. Dmitriev, Yu. M. Mukharsky, E. V. Poddyakova, and O. D. Timofeevskaya, Zh. Eksp. Teor. Fiz. **96**, 956 (1989) [Sov. Phys. JETP **69**, 42 (1989)], and references therein.

[16] Y. Kondo, J. S.Korhonen, M. Krusius, V. V. Dmitriev, Yu. M. Mukharsky, E. B. Sonin, and G. E. Volovik, Phys. Rev. Lett. **67**, 81 (1991).

[17] A. L. Fetter, in *The Physics of Liquid and Solid Helium*, edited by K. H. Bennemann and J. B. Ketterson (Wiley, New York, 1976), Part I, Chap. 3.

[18] A. R. Ashton and W. I. Glaberson, Phys. Rev. Lett. **42**, 1062 (1979).

[19] R. E. Packard and T. M. Sanders, Jr., Phys. Rev. A **6**, 799 (1972).

[20] E. J. Yarmchuk and R. E. Packard, J. Low Temp. Phys. **46**, 479 (1982).

[21] Y. Kondo, J. S. Korhonen, Ü. Parts, M. Krusius, O. V. Lounasmaa, and A. D. Gongadze, Physica B **178**, 90 (1992); Ü. Parts, P. I. Soininen, M. Fogelström, Yu. M. Bunkov, V. V. Dmitriev, Y. Kondo, J. S. Korhonen, N. B. Kopnin, and M. Krusius (unpublished).

[22] E. B. Sonin, Zh. Eksp. Teor. Fiz. **70**, 1970 (1976) [Sov. Phys. JETP **43**, 1027 (1976)].

[23] This regime has been studied by A. F. Andreev and M. Yu. Kagan, Zh. Eksp. Teor. Fiz. **86**, 546 (1984) [Sov. Phys. JETP **59**, 318 (1984)]. They call it "fast rotation."

[24] S. D. Tsakadze, Zh. Eksp. Teor. Fiz. **71**, 754 (1976) [Sov. Phys. JETP **44**, 398 (1976)].

[25] V. K. Tkachenko, Zh. Eksp. Teor. Fiz. **49**, 1875 (1965) [Sov. Phys. JETP **22**, 1282 (1965)].

[26] A. I. Larkin and Yu. N. Ovchinnikov, J. Low Temp. Phys. **43**, 408 (1979).

[27] H. E. Hall, Adv. Phys. **9**, 89 (1960).

[28] V. K. Tkachenko, Zh. Eksp. Teor. Fiz. **50**, 1573 (1966) [Sov. Phys. JETP **23**, 1049 (1966)].

[29] I. A. Fomin, in *Helium Three Modern Problems in Condensed Matter Physics*, edited by W. P. Halperin and L. P. Pitaevskii (North-Holland, Amsterdam, 1990), Vol. 26, p. 610.

[30] D. Vollhardt, K. Maki, and N. Schopohl, J. Low Temp. Phys. **39**, 79 (1980).

[31] P. J. Hakonen, M. Krusius, M. M. Salomaa, R. H. Salmelin, J. T. Simola, A. D. Gongadze, G. E. Vachnadze, and G. A. Kharadze, J. Low Temp. Phys. **76**, 225 (1989).

[32] H. N. Scholz, Ph. D. thesis, Ohio State University, 1981 (unpublished).

[33] J. S. Korhonen, Yu. M. Bunkov, V. V. Dmitriev, Y. Kondo, M. Krusius, Yu. M. Mukharsky, Ü. Parts, and E. V. Thuneberg, Phys. Rev. B **46**, 13 983 (1992).

[34] Y. Kondo, J. S. Korhonen, and M. Krusius, Physica B **165&166**, 673 (1990).

[35] D. D. Awschalom and K. W. Schwarz, Phys. Rev. Lett. **52**, 49 (1984).

[36] D. Stauffer and A. L. Fetter, Phys. Rev. **168**, 156 (1968).

[37] L. J. Campbell and R. M. Ziff, Phys. Rev. B **20**, 1886 (1979).

[38] H. E. Hall and W. F. Vinen, Proc. R. Soc. London, Ser. A **238**, 204 (1956).

[39] H. Lamb, *Hydrodynamics* (Dover, New York, 1945).

[40] R. J. Zieve, Yu. Mukharsky, J. D. Close, J. C. Davis, and R. E. Packard, Phys. Rev. Lett. **68**, 1327 (1992).

[41] C. F. Barenghi, R. J.Donnelly, and W. F. Vinen, J. Low Temp. Phys. **52**, 189 (1983).

[42] N. B. Kopnin and M. M. Salomaa, Phys. Rev. B **44**, 9667 (1991).

[43] L. P. Gor'kov and N. B. Kopnin, Usp. Fiz. Nauk **116**, 413 (1975) [Sov. Phys. Usp. **18**, 496 (1975)].

[44] V. L. Ginzburg and A. A. Sobyanin, J. Low Temp. Phys. **49**, 507 (1982).

[45] E. B. Sonin, J. Low Temp. Phys. **42**, 417 (1981).

[46] N. B. Kopnin, Zh. Eksp. Teor. Fiz. **74**, 1538 (1978) [Sov. Phys. JETP **47**, 804 (1978)].

[47] E. B. Sonin, Pisma Zh. Eksp. Teor. Fiz. **43**, 601 (1986) [JETP Lett. **43**, 779 (1986)].

[48] H. E. Hall, P. L. Gammel, and J. D. Reppy, Phys. Rev. Lett. **52**, 1701 (1984).

[49] H. P. Greenspan, *The Theory of Rotating Superfluids* (Cambridge University Press, Cambridge, 1968).

[50] E. B. Sonin, Physica B **178**, 106 (1992).

[51] M. A. Alpar and K. S. Cheng, J. Low Temp. Phys. **60**, 415 (1985).

[52] P. J. Hakonen and V. P. Mineev, J. Low Temp. Phys. **67**, 313 (1987).

[53] E. L. Andronikashvili and Yu. G. Mamaladze, in *Progress in Low Temperature Physics,* edited by C. J. Gorter (North-Holland, Amsterdam), Vol. 5, p. 79.

[54] M. A. Alpar, J. Low Temp. Phys. **31**, 803 (1978).

[55] J. S. Tsakadze and S. J. Tsakadze, Usp. Fiz. Nauk. **115**, 503 (1975) [Sov. Phys. Usp. **18**, 242 (1975)].

[56] E. B. Sonin, A. K. Tagantsev, and K. B. Traito, Phys. Rev. B **46**, 5830 (1992).

[57] M. L. Bekarevich and I. M. Khalatnikov, Zh. Eksp. Teor. Fiz. **40**, 920 (1961) [Sov. Phys. JETP **13**, 643 (1961)].

[58] I. M. Khalatnikov, *Introduction to the Theory of Superfluidity* (Benjamin, New York, 1965).

[59] S. J. Tsakadze, Zh. Eksp. Teor. Fiz. **71**, 754 (1976) [Sov. Phys. JETP **44**, 398 (1976)].

[60] E. J. Yarmchuk and W. I. Glaberson, Phys. Rev. Lett. **41**, 564 (1978); J. Low Temp. Phys. **36**, 381 (1979); S. G. Hedge and W. I. Glaberson, Phys. Rev. Lett. **45**, 190 (1980).

[61] S. J. Tsakadze, Fiz. Nizk. Temp. **4**, 148 (1978); J. S. Tsakadze, S. J. Tsakadze, and E. B. Sonin, Phys. Rev. B **21**, 3028 (1980).

[62] L. J. Campbell, Phys. Rev. Lett. **43**, 1336 (1979).

[63] J. S. Tsakadze and S. J. Tsakadze, J. Low Temp. Phys. **39**, 649 (1980).

[64] K. C. Harvey and A. L. Fetter, J. Low Temp. Phys. **11**, 473 (1973).

[65] T. Ohmi, T. Tsuneto, and T. Usui, Prog. Theor. Phys. **41**, 1395 (1969).

[66] Ü. Parts, Y. Kondo, J. S. Korhonen, M. Krusius, and E. V. Thuneberg (unpublished).

[67] P. L. Marston and W. M. Fairbank, Phys. Rev. Lett. **39**, 1208 (1977).

[68] M. Ruderman, Nature (London) **225**, 619 (1970).

[69] M. R. Williams and A. L. Fetter, Phys. Rev. B **16**, 4846 (1977).

[70] L. J. Campbell, Phys. Rev. A **24**, 524 (1981).

[71] E. B. Sonin, Y. Kondo, J. Korhonen, and M. Krusius, *Proceedings of the International Conference on Low Temperature Physics LT20* [Physica B (to be published).]